Impact of crust–mantle mechanical coupling on the topographic and thermal evolutions during the necking phase of 'magma-poor' and 'sediment-starved' rift systems: A numerical modeling study

Pauline Chenin, Stefan M Schmalholz, Gianreto Manatschal, Thibault Duretz

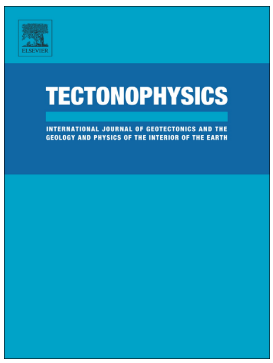

Impact of crust–mantle mechanical coupling on the topographic and thermal evolutions during the necking phase of 'magma-poor' and 'sediment-starved' rift systems: A numerical modeling study

Pauline Chenin, Stefan M. Schmalholz, Gianreto Manatschal, Thibault Duretz

PII: S0040-1951(20)30155-4

DOI: https://doi.org/10.1016/j.tecto.2020.228472

Reference: TECTO 228472

To appear in: *Tectonophysics*

Received date: 2 August 2019

Revised date: 30 April 2020

Accepted date: 4 May 2020

Please cite this article as: P. Chenin, S.M. Schmalholz, G. Manatschal, et al., Impact of crust–mantle mechanical coupling on the topographic and thermal evolutions during the necking phase of 'magma-poor' and 'sediment-starved' rift systems: A numerical modeling study, *Tectonophysics* (2019), https://doi.org/10.1016/j.tecto.2020.228472

Impact of crust–mantle mechanical coupling on the topographic and thermal evolutions during the necking phase of 'magma-poor' and 'sediment-starved' rift systems: a numerical modeling study

Pauline Chenin[a], Stefan M. Schmalholz[b], Gianreto Manatschal[a], Thibault Duretz[c]

[a] *CNRS–IPGS–Université de Strasbourg, 1 Rue Blessig, 67084 Strasbourg, France*

[b] *Institut des Sciences de la Terre–Université de Lausanne, Bâtiment Géopolis CH-1015 Lausanne, Switzerland*

[c] *CNRS–Géosciences-Rennes–Université de Rennes, BAT 14B, Campus Beaulieu, 35042 Rennes, France*

Pauline Chenin: Investigation and Conceptualization, Writing - Original Draft. Stefan Schmalholz: Conceptualization, Writing - Review & Editing, Resources. Gianreto Manatschal: Conceptualization, Writing - Review & Editing, Funding acquisition. Thibault Duretz: Software, Conceptualization, Writing - Review & Editing

Corresponding author

Email address: chenin@unistra.fr (Pauline Chenin)

Abstract

We used high-resolution (500 x 250 m) two-dimensional lithospheric-scale thermo-mechanical numerical modeling to unravel the unexpected topographic and thermal evolutions recorded during the necking phase of several rift systems worldwide. Through a systematic analysis we studied how the lithosphere rheology impacts the topographic and thermal evolutions across the entire width of magma-poor and sediment-starved rift systems until their crust is locally thinned to 10 km. We quantified the evolution of topography, uplift and subsidence rates, accommodation and emerged space creation, temperature and surface heat flow for a wide panel of crustal and mantle rheologies to provide an overview of possible rifting behaviors. Extension of a lithosphere for which the crust and mantle are mechanically decoupled by a weak lower crust generates complex morphotectonic evolutions, with the formation of temporarily restricted sub-basins framed by uplifted parts of the future distal margin. Mechanical decoupling between the crust and mantle controls also largely the thermal evolution of rift systems during the necking phase since, for equivalent extension rates and initial geotherms: (i) weak/decoupled lithospheres have a higher geothermal gradient at the end of the necking phase than strong/coupled lithospheres; and (ii) weak/decoupled lithospheres show intense heating of the lower crust at the rift center and intense cooling of the crust on either side of the rift center, unlike strong/coupled lithospheres. These behaviors contrast with the continuous subsidence and cooling predicted by the commonly used depth-uniform thinning model. Accommodation space in the evolving basins is first generated by vertical crustal velocities and subsequently by horizontal velocities causing the widening of the earlier formed basin. Processes such as strain softening and mantle fertilization have a limited impact on the primary morphology and thermal state of rift systems before the crust is thinned to 10 km but may locally amplify relief and thermal heterogeneities.

Keywords: rift, necking, topographic evolution, thermal evolution, numerical modeling

1. Introduction

The formation of sedimentary basins and the subsidence recorded at rift systems have been attributed to lithosphere necking and thinning processes since the early 1970's (e.g. Artemjev & Artyushkov, 1971). McKenzie (1978) developed a simple but robust model to explain the subsidence and temperature evolutions of sedimentary basins formed in extensional settings, assuming that lithosphere thinning is instantaneous and uniform with depth (Figure 1a). In this so-called *depth-uniform thinning (DUT) model*, extension of a lithosphere generates (black curves in Figures 1b and 1c): (ia) immediate surface subsidence related to crustal thinning together with (ib) instantaneous geothermal gradient increase without any material heating (the lithospheric material is simply advected upward); subsequently, thermal relaxation results in (iia) progressive surface subsidence as a result of (iib) lithosphere cooling.

The DUT model has been successfully applied to describe the subsidence and thermal evolutions of rift basins that developed over a crust–lithosphere that underwent little thinning, for instance in the proximal domain of rifted margins where the ratio of initial to final crustal thickness β is less than 1.3 (White & McKenzie, 1989; Hendrie et al., 1993). However, Royden & Keen (1980) showed that the DUT model cannot explain the subsidence history recorded at distal parts of rifted margins and argued for differential crust and mantle thinning (i.e. depth-dependent thinning, DDT). Recent data from distal parts of rifted margins provide growing evidence for a complex tectono-thermal evolution during the *necking phase* of rifting (i.e. when the crust is thinned from 30–35 to ca. 10 km; Sutra et al., 2013). For example, the Tithonian shallow-water carbonates and clays drilled at ODP Sites 901, 1065 and 1069 offshore Iberia suggest that the distal domain of the Iberian margin remained at shallow water depths during advanced stages of rifting (Mohn et al., 2014). This subsidence evolution is schematically represented as the red curve in Figure 1b.

In some rift systems, distal domains show an initial phase of rift-related subsidence, which is followed by a phase of erosion and/or emersion, and subsequently a phase of renewed subsidence. For instance, the Briançonnais domain in the fossil distal European margin of the Alpine Tethys (e.g. Claudel & Dumont, 1999, Figure 1d), the Campos Basin offshore Brazil (Lewis et al., 2014), the South China Sea (e.g. Lin et al., 2003) and the East India margin (Haupert et al., 2016) show such a subsidence–uplift/emersion–subsidence evolution. The width of the

karstified/emerged domain in the Briançonnais can be roughly estimated to a few tens of kilometers based on present-day mapping of the corresponding formation. However, the width of the karst varies largely along strike and its estimate depends on the assumptions made on the direction of Alpine compression. The extent of the erosional unconformity is better constrained in the outer hinge of the Campos Basin, where it was mapped over a width of 10–30 km over 120 km along strike (Lewis et al., 2014). The subsidence–uplift/emersion–subsidence evolution recorded by these margins is schematically represented by the blue curve in Figure 1b.

The thermal evolution of continental crust during rifting is difficult to assess due to the lack of access to deep crustal levels, especially at present-day rifted margins. Currently, the only clues are thermochronological data from fossil rifted margins exposed in the Alps and Pyrenees. In both cases data indicate a transient but intense syn-rift heating event at the base of the continental crust (prograde metamorphism), which predates the phase of subcontinental mantle exhumation (Smye & Stockli, 2014; Seymour et al., 2016; Hart et al., 2017). In the Alps, this thermal event was dated to 200–179 Ma (Beltrando et al., 2015), and thus was largely contemporaneous with the necking phase dated between 189 and 179 Ma by Mohn et al. (2012) and between 191 and 185 Ma by Ribes et al. (2019). The thermal evolution recorded at the base of the crust in the distal domain of the Alpine and Pyrenean rift systems is schematically represented by the blue curve in Figure 1c.

Figure 1: a) Illustration of the depth-uniform thinning model from McKenzie (1978); abbreviations: cont.: continental, lithos.: lithospheric; astheno.: asthenospheric mantle. b) Schematic graph showing the topographic evolution of the distal part of different types of rift systems; c) Schematic graph showing the thermal evolution at the base of the crust in the distal part of different types of rift systems. d) Annotated photograph showing the stratigraphic relationships in the Briançonnais unit (Alps of southeastern France). The Briançonnais unit belonged to the distal European margin of the former Alpine Tethys rift system.

Several processes may account for both delayed subsidence, and even emersion, and a heat pulse at the base of the crust during rifting. These include:

- simple shear-dominated extension (e.g. Wernicke, 1985; Lemoine et al., 1987), where one lithospheric-scale shear zone causes a lateral offset in crustal and mantle thinning. This process can account for both uplift and transient crustal heating at *one* distal margin of a rift

system;

- depth-dependent thinning (e.g. Royden & Keen, 1980; Roberts et al., 1997; Driscoll & Karner, 1998; Kusznir & Karner, 2007; Huismans & Beaumont, 2011), where higher lithospheric than crustal thinning results in transient uplift and local heating of the lower crust during rift-related extension;
- magmatic underplating (e.g. White & McKenzie, 1989), where addition of hot and low-density material beneath the crust may result in local uplift and heating;

The following processes may explain distal margin uplift but do not account for a transient and/or local heating event:

- flexural processes (Braun & Beaumont, 1989; Kooi et al., 1992; Weissel & Karner, 1989; Chenin et al., 2019), where isostatic movements caused by the thinning of a lithosphere with a significant flexural rigidity result in uplift (or subsidence) of parts of the margin. For instance, flexural rift shoulder uplift is important in numerical models with strain softening (e.g. Svartman Dias et al., 2015; Huismans & Beaumont, 2011);
- surface processes, whereby mass redistribution related to erosion and sedimentation causes loading and subsidence or unloading and uplift of specific parts of rift systems (e.g. Burov & Poliakov, 2001, 2003);
- dynamic topography (e.g. White & McKenzie, 1989; Xie et al., 2006), where regions of high- (mantle plumes) or low (subduction-related) temperatures within the asthenospheric mantle cause large-scale and long-lasting uplift or subsidence, respectively;
- removal of the continental mantle lithosphere (i.e. 'delamination') prior to continental breakup (e.g. Leeds et al., 2012), where replacement of lithospheric mantle by lower density asthenospheric mantle results in transient, large-scale uplift and heating of the lower crust.
- mineral phase changes (e.g. Kaus et al., 2005; Simon & Podladchikov, 2008), where the density decrease associated with the transition from garnet- to plagioclase-peridotite at relatively low pressure and high temperature leads to uplift of the most distal part of the rift basin during advanced stages of crustal thinning;
- serpentinization (e.g. Reston et al., 2001), where the increased volume and lower density of serpentinized peridotite with respect to fresh peridotite causes uplift in the most distal part of the rift basin;

However, many of these processes fail accounting for one or several characteristics of the rift systems mentioned above:

- Simple shear-dominated extension may explain asymmetric topographic and thermal evolutions of rift systems since the upper plate is heated and uplifted with respect to the lower plate. However, applied to the necking stage, this model implies highly-localized, simple shear deformation across the lithosphere, which is incompatible with the distributed extension generally observed during the early stages of rifting (e.g. Withjack et al., 2012; Ball et al., 2013; Beltrando et al., 2015);
- Magmatic underplating is accompanied by extensive syn-rift magmatic activity, which are not observed during 'magma-poor' rifting.
- Dynamic topography and delamination of the continental lithosphere induce typically a large-scale uplift (several hundred kilometers in diameters; e.g. Campbell (2005); Esedo et al. (2012)), which could theoretically result in local erosion depending on the morphology of the margin. However, this process cannot account for the few tens of kilometers wide erosion of the future distal domain observed in the East India, South China Sea and Brazilian margins and in the former European margin of the Alpine Tethys because the adjacent proximal domains, which were made of thick continental crust and thus rested at shallow water depths, escaped erosion during the uplift of the future distal margin (Haupert et al., 2016; Lin et al., 2003; Lewis et al., 2014; Bourbon, 1980).
- Several numerical models show that flexural processes may produce uplift above sea level around the so-called 'rift shoulders' on either side of the rift basin. However, these uplifts are usually limited to the proximal part of rift systems (e.g. Huismans & Beaumont, 2011; Svartman Dias et al., 2015), independent on whether or not erosion and/or sedimentation are modeled (Burov & Poliakov, 2001, 2003).
- According to Kaus et al. (2005); Simon & Podladchikov (2008); Reston et al. (2001), the garnet- to plagioclase-peridotite transition as well as the serpentinization processes can account for up to hundreds of meters uplift of distal parts of a rift system. However, these processes are restricted to advanced stages of crustal thinning (i.e. when the crust is less than 10 km thick), and thus cannot account for uplift during the earlier necking phase of rifting.

From the above arguments, it appears that DDT is a process that could account for a

transient uplift limited to the future distal domain during the necking phase of a magma-poor rift system. The characteristics of DDT are essentially controlled by the rheology of the lithosphere (Huismans & Beaumont, 2014; Chenin et al., 2018), which depends on the lithology and distribution of the different lithospheric materials, as well as on the initial geothermal gradient.

Since the 1980's, many studies have highlighted the impact of the lithosphere rheology on the timing of rifting, as well as on the thermal evolution and final morphology of rift systems (e.g. Buck, 1991; Bassi, 1991, 1995; Cloetingh et al., 1995; Gartrell, 2001). However, a systematic and quantitative analysis of the impact of the initial rheology on the topographic and thermal evolutions of rift systems is lacking to date. In particular, such quantification requires high-resolution numerical models with accurate free surface tracking and up-to-date rheological models, which were only developed over the last decade (e.g. Popov & Sobolev, 2008; Thieulot, 2011; Duretz et al., 2016a; Vogt et al., 2018). Besides, most studies focused on the topographic and thermal evolutions of the rift center, and much less attention was paid to the evolution of surface topography and temperature across the entire width of rift domains (exceptions are Van Wijk & Cloetingh (2002), their Figure 9; and Watremez et al. (2013), their Figures 4 and 5).

Our study aims to provide insight into the variability of the topographic and thermal evolutions of extensional systems in order to explain the particular erosional features and the heat pulse recorded during the necking phase of several rift systems worldwide. We perform a systematic numerical study with high-resolution simulations (i.e. 500 x 250 m resolution in models that include the entire lithosphere thickness and the upper 75 km of the asthenosphere). We consider a simple lithospheric rheological architecture with homogeneous visco-elasto-plastic crust and mantle. To model the mantle lithosphere we use state-of-the-art rheological models, which consist of a combination of diffusion, dislocation and Peierls creep together with pressure-dependent plasticity and elasticity. We focus on the mechanical coupling/decoupling of the lithosphere and associated DDT by testing various crustal and mantle flow laws. Our aims are (1) to quantify the spatio-temporal evolution of topography, uplift/subsidence rates, accommodation/emerged space creation, temperature and surface heat flow; (2) to understand the relation of these evolutions to deeper lithosphere processes such as necking and flexure of the mantle lithosphere; and (3) to evaluate the impact of additional processes such as prominent normal faulting, modeled by strain softening, and mantle fertilization.

2. Model Configuration

We use the two-dimensional finite difference/marker-in-cell thermo-mechanical code MDoodz to model lithospheric extension, which was applied also in Duretz et al. (2016b), Petri et al. (2019) and Duretz et al. (2020). The model considers visco-elasto-plastic incompressible deformation, strain-rate-, stress- and temperature-dependent rheologies and thermo-mechanical coupling by shear heating. We apply a diffusion-type erosion-sedimentation model with a diffusion coefficient $K = 5.0 \times 10^{-6}$ $m^2 \cdot s^{-1}$. Unless stated otherwise we do not apply strain softening or mineral phase changes.

The model domain (Figure 2) is 300 km-wide and 200 km-deep with a resolution of 500 m horizontally and 250 m vertically. The top boundary is a free surface (Duretz et al., 2016a), while free slip is applied to the left, right and bottom boundaries. Horizontal velocities (v) at both vertical model sides are in the order of 1 $cm \cdot yr^{-1}$. These velocities are adjusted by the current model width (W) to generate a constant bulk extension rate ($\dot{\varepsilon}$) of 1×10^{-15} s^{-1} ($\dot{\varepsilon} = 2v / W$). The model surface topography is a material interface defined by a high-resolution Lagrangian marker chain, which is displaced with the numerically calculated velocity field.

The modeled lithosphere comprises an initially 30 km-thick continental crust overlying a 95 km-thick upper mantle and a 75 km-thick adiabatic mantle (see next paragraph). To trigger localization of the deformation, we perturb the initial depth of the crust-mantle boundary with a sinusoidal function having a 2.5 km amplitude and a 300 km wavelength, so that the geometrical perturbation is smoothly distributed over the entire model width. We counterbalance the Moho perturbation by a sinusoidal surface topography of ca. 0.5 km amplitude and 300 km wavelength, so that our models are initially in isostatic equilibrium. Chenin et al. (2018) showed that the wavelength of the sinusoidal Moho perturbation has little impact on both the duration of the necking phase and the width/morphology of the necking zones (see first paragraph of their section 4.2). Similarly, using a weak seed instead of a sinusoidal perturbation of the Moho depth has limited effects on the rift evolution (compare figures B4e and B4f in Chenin et al. (2019)), which is consistent with the conclusions of Huismans & Beaumont (2007).

The temperature is 0 °C at the top of the model, 1330 °C within the asthenosphere and zero heat flux is imposed to the model vertical sides. The crust has a constant radiogenic heat production of 1 $\mu W \cdot m^{-3}$. To mimic adiabatic mantle temperatures, we compute the initial

temperature field using an unrealistically large asthenosphere conductivity of 3000 $W \cdot m^{-1} \cdot K^{-1}$. During the simulation, the conductivity is set back to 3 $W \cdot m^{-1} \cdot K^{-1}$. This set up results in slow diffusive cooling of the lithosphere–asthenosphere boundary, which has however no significant impact given the short duration of the simulation ($\leq$ 8 My). The initial Moho temperature in the model center is 550 °C, consistent with the 550–600 °C temperatures at the base of the crust at the onset of the Alpine Tethys rifting reckoned by Müntener et al. (2000).

We investigate the impact of lithosphere rheology by first testing various flow laws for both the crust and the mantle. We distinguish between two Model Series, namely Series D and W. The models of Series D have a dry olivine mantle (strong rheology), while the crust varies from Maryland diabase (Model D1; extremely strong crust) to wet quartz (Model D6; extremely weak crust; see Figure 2 for the intermediate rheologies tested). The models of series W have a wet olivine mantle (weaker than dry olivine) and we test the same range of crustal rheologies as in Series D, naming the models accordingly (Models W1–W6). The physical properties of each material are summarized in Table 1.

Second, with Model Series D5+, we test the effect of additional parameters/processes such as the type(s) of creep included in the mantle flow law (diffusion creep and Peierls creep), mantle fertilization and strain softening. The models of Series D5+ have a similar initial rheology as Model D5 (dry quartz continental crust, dry olivine mantle). In Models D5+No diffusion creep, D5+No Peierls creep and D5+No diffusion & no Peierls creep we test the effect of removing diffusion and/or Peierls creep from the mantle flow law (see Table 1). In Model D5+Fertilization, we model the density decrease associated with mantle fertilization by melt impregnation (Müntener et al., 2010; McCarthy & Müntener, 2015). To mimic the transition from an inherited harzburgite to a fertile plagioclase peridotite, we decrease the density of the mantle from 3330 to 3200 $kg \cdot m^{-3}$ (i.e. densities of 'inherited' and 'fertile' mantle according to Chenin et al. (2017)) when the temperature is above 1050 °C and the pressure below 1 GPa (equilibration pressure and temperature of the plagioclase peridotite from Müntener et al. (2010)). Finally, in Models D5+Softening and D5+Softening CC, we test the impact of intense strain softening by decreasing linearly the internal angle of friction from 30 ° to 5 ° and the cohesion from 10 to 1 MPa when accumulated plastic strain increases from 5 % to 20 %, after which both the internal angle of friction and the cohesion remain constant. Strain softening is considered in both the crust and the mantle in Model D5+Softening and limited to the crust in Model D5+Softening CC.

We limit our numerical modeling investigations to the stages where crustal thickness remains larger than 10 km because we aim to quantify the evolutions of topography and temperature systematically and in detail during the necking phase of rifting only.

Figure 2: Model configuration with depth-dependent stress profile and geothermal gradient at the model center for the different rheologies tested. The right-hand side stress profile zooms on the shallowest 100 km of the lithosphere. Each crustal and mantle material is associated to a bracketed number (from 1 to 6) or letter (W or D), which are used to reference the simulations (for instance Model W1 is made of wet olivine mantle and Maryland diabase crust).

Table 1: Material physical properties and flow law parameters. Flow law parameters for Maryland diabase are from Mackwell et al. (1998); mafic and felsic granulite from (Ranalli, 1995); $Anorthite_{60}$ from Rybacki & Dresen (2004); dry and wet quartz from Ranalli (1995, 1997); olivine (dry and wet) dislocation and diffusion creep from Hirth & Kohlstedt (2003); olivine (dry and wet) Peierls creep from Evans & Goetze (1979) using the approach from Kameyama et al. (1999).

	Crust	Mantle	Sediments
density ρ $(kg \cdot m^{-3})$	2800	3330	2300
internal angle of friction ϕ $(^{\circ})$	30	30	30
cohesion C_0 (MPa)	10	10	10
heat capacity C_p $(J \cdot kg^{-1} \cdot K^{-1})$	1050	1050	1050
thermal conductivity k $(W \cdot m^{-1} \cdot K^{-1})$	2.5	3.0	2.0
heat production H $(\mu W \cdot m^{-3})$	1.0	0.0	0.5
thermal expansion α $(^{\circ}C^{-1})$	3.2×10^{-5}	3.2×10^{-5}	1.0×10^{-5}
compressibility β (Pa^{-1})	1.5×10^{-11}	1.5×10^{-11}	1.5×10^{-11}.

Crustal material dislocation creep parameters			
	n	Q	A
		$(kJ \cdot mol^{-1})$	$(Pa^{-n} \cdot s^{-1})$
Maryland diabase	4.7	485	5.0477×10^{-28}

Mafic granulite	4.2	445	8.8334×10^{-22}
Felsic granulite	3.1	243	2.0095×10^{-21}
Anorthite$_{60}$	3.0	235	3.16228×10^{-20}
Dry quartz	2.4	156	2.667×10^{-20}
Wet quartz and sediments	2.3	154	5.0717×10^{-18}

Mantle flow law parameters	Dry olivine	Wet olivine
Dislocation creep		
Stress exponent n	3.5	3.5
Activation energy Q (kJ·mol^{-1})	530	480
Pre-exponential constant A (Pa^{-n}·s^{-1})	1.1×10^{-16}	5.6786×10^{-27}
Activation volume V^* (m^3·mol^{-1})	1.1×10^{-5}	1.1×10^{-5}
Water fugacity f (MPa)	0	1.0×10^{9}
Water fugacity exponent r	0	1.2
Diffusion creep		
Stress exponent n	1	1
Grain size exponent m	3	3
Activation energy Q (kJ·mol^{-1})	375	375
Pre-exponential constant A (Pa^{-n}·s^{-1})	1.5×10^{-15}	2.5×10^{-23}
Activation volume V (m^3·mol^{-1})	4.0×10^{-6}	7.0×10^{-6}
Water fugacity f (MPa)	0	1.0×10^{9}
Peierls creep		
Stress dependence q	2.0	2.0
An adjustable constant γ	0.1	0.1
Peierls stress σ_p (Pa)	8.5×10^{9}	8.5×10^{9}
Activation energy Q (kJ·mol^{-1})	540	540
Pre-exponential constant A_p (s^{-1})	5.7×10^{11}	5.7×10^{11}

3. Results

3.1. Impact of Crustal and Mantle Rheology

Figure 3 summarizes the surface topography (panels a and b), simulation duration (panel c) and thermal state (panels d, e and f) of Model Series D (dry olivine mantle) and W (wet olivine mantle) at the end of the necking stage. Four systematic trends stand out: (1) the stronger the crust, the larger the relief (Figures 3a and 3b); (2) the stronger the crust, the shorter the duration of the necking phase (Figure 3c); (3) for comparable crustal rheologies the duration of the necking phase is consistently shorter by 0.6 to 0.9 My in the models of Series W than in those of Series D (Figure 3c); and (4) the stronger the crust, the deeper the 500 and 1300 °C isotherms at the end of the simulation, and thus the lower the geothermal gradient (Figures 3d and 3e).

In contrast, no systematic trend can be identified between crustal rheology and the maximum surface heat flow at the end of the simulation (Figure 3f). In Model Series W, the maximum heat flow is consistently relatively low (between 170 and 220 $mW \cdot m^{-2}$), regardless of crustal rheology. In Model Series D, the maximum heat flow varies between 190 and 260 $mW \cdot m^{-2}$ regardless of crustal strength.

The rheology of the mantle impacts the characteristics of rift systems to a variable extent: when the crust is strong (Maryland diabase or Mafic granulite rheology), the relief of the rift system at the end of the necking phase is larger by ca. 3 km in Series D than in the equivalent models of Series W; however, for weaker crustal rheologies, the relief is relatively similar amongst the equivalent models of the two series (Figures 3a and 3b). The rheology of the mantle does not control the depth of the 1300 °C isotherm in the rift center at the end of the necking phase, since it is comprised between 30 and 90 km in both Series (Figure 3e). However, the rheology of the mantle impacts the depth of the 500 °C isotherm in such a way its depth range is narrower in the models of Series W (8–16 km) than in those of Series D (6–18 km depth; Figure 3d).

Figure 3: a) and b) Surface topography at the end of the simulation (i.e. when the crust is locally thinned to 10 km) of Model Series D (dry olivine mantle) and Model Series W (wet olivine mantle), respectively. c) Necking duration of the different models of Series D (squares) and W (circles); d) and e) Minimum depth of the 500 and 1300 °C isotherms, respectively, at the end of the simulation in Model Series D and W; f) Maximum surface heat flow at the end of the

simulation in Model Series D and W.

3.1.1. Topographic Evolution

3.1.1.1 Strong Crust Models. When the crust is strong and thus largely mechanically coupled with the underlying mantle (Models D1, D2, W1 and W2; Figures 4a, 4b, A.15a, A.15b, A.15g and A.15h), the rift consists of one single basin with steep edges during the entire simulation. In the four models, the basin deepens rapidly as extension progresses, reaching up to 9.5 km at the end of the simulation in Model D1. At the same time, high rift shoulders grow up to 3 km in Model D1. As the rift basin is deep, the underlying Moho is also deep at the end of the simulation (up to ca. 19.5 km in Model D1; Figure 4a). Crustal thinning to 10 km is completed in less than 4.5 My in the four models (Figure 3c). There is no significant difference in the evolution of models with a strong versus a weak mantle except that the rift basin, and thus the Moho, are slightly shallower in the models with a weaker mantle (basin depth is 7.5 km and 9.5 km in Model W1 and D1, respectively; compare Figures 3a and 3b).

Figure 4: Top panels: surface (magenta curve), top basement and Moho topography (black curves) at the end of the necking phase (i.e. when the crust is locally thinned to 10 km). The space between the magenta and top basement curves represents sediments. The horizontal blue line corresponds to the isobath 0 km. The 500 °C (and in panels e and f the 1300 °C) isotherms are plotted in red. Bottom panels: evolution of surface topography with time along different models. RS: Rift Shoulder.

3.1.1.2 Moderately Strong to Weak Crust and Strong Mantle Models (Series D). When the mantle is strong and the crust moderately strong to weak (Model D3: felsic granulite to D6: wet quartz; Figures 4c, 4e and A.15c–f), three sub-basins separated by two relative highs form from approximately 2 My onward. In Models D3 and D4 (moderately strong crust), the central sub-basin remains largely shallower (ca. 0.5–1 km-deep) than those on either side (ca. 1.5–2 km-deep) until approximately three quarters of the necking duration (Figures 4c, A.15c and A.15d). During the last quarter of the simulation the central sub-basin subsides rapidly, reaching a depth of 3 km at the end of Model D3 (Figure 3a). At the same time, the relative highs on either side rise, reaching a depth of ca. 500 m at the end of Model D4 (ca. 250 m in Model D3).

In Models D5 and D6, where the crust is weaker (dry and wet quartz, respectively), the central sub-basin forms and remains deeper than or as deep as those on either side until approximately half of the necking duration (900 m in Model D5, 500 m in Model D6; Figures 4e and A.15e–f). During the third quarter of the simulation, the depth of the central sub-basin decreases by approximately 300 m, reaching 600 m in Model D5 and 300 m in Model D6. During the last quarter of the simulation, the central sub-basin subsides rapidly, reaching its maximum depth at the end of the simulation (200-300 m in Model D5 and less than 100 m in Model D6). At the same time, the relative highs on either side are transitorily uplifted to less than 100 m depth in Model D5, hence above sea level in Model D6. In Models D3 to D6, the central basin remains isolated from the adjacent ones during most of the necking phase because of the two highs framing it (Figures 4c, 4e and A.15c–f).

3.1.1.3 Moderately Strong to Weak Crust and Weak Mantle Models (Series W). Comparison between Models W3–W6 (wet olivine mantle) and Models D3–D6 (dry olivine mantle) highlights that the topographic evolution of models differing by only their mantle strength may vary significantly (Figures 4c–f, A.15c–f and A.15i–l). The behavior of Model W3 is close to that of Models D1, D2, W1 and W2 in that one single rift basin forms and subsides continuously. Although the depth of the main rift basin at the end of the simulation is similar in models D3 and W3 (ca. 3.1 km), the basin edges dip gently and regularly toward the basin center in Model W3, while the topography is much more bumpy in Model D3 (compare panels c and d in Figure 4 and green profiles in panels a and b of Figure 3).

In Models W4 and W5, only two sub-basins form on either side of one single relative high in the model center, which contrasts with the three sub-basins of Models D3–D6 (Figures 4c, 4f and A.15j–l). The central high of Models W4 and W5 remains at a shallow depth of 100–300 m compared to the 1–1.5 km-deep adjacent sub-basins until approximately three quarters of the necking phase. The central high of Models W3 and W4 remains also at shallower depth than the 600 and 300 m-deep distal highs of Models D4 and D5, respectively (Figure 4e A.15d and A.15e). During the last quarter of the simulation, the central high is split in two as a new sub-basin forms in its center and subsides rapidly to ca. 2 km depth in Models W4 and W5. At the same time, the two outer sub-basins become shallower (1.1–1.2 km in Model W4, 600–700 m in Model W5).

The evolution of Model W6 differs from that of the other models in that four shallow

(100–500 m deep) sub-basins separated by three relative highs (< 100 m deep) form and persist until 5.5 My (approximately three quarters of the necking duration; Figure A.15l). Extension focuses eventually in the second basin to the right, which reaches only 1 km depth when crustal necking is achieved at 7.4 My.

3.1.1.4 Summary. We identify four types of topographic evolution for the necking phase of a rift system: (1) formation of one single, narrow and deep rift basin that subsides continuously and rapidly (Models D1, D2 and W1–W3); (2) formation of three sub-basins separated by two distal highs within the main rift basin; the distal highs may record transient uplift at various stages of the necking phase (Models D3–D6); (3) formation of two sub-basins separated by one distal high within the main rift basin; subsidence of the distal high is delayed to late stages of the necking phase (Models W4 and W5); and (4) formation of multiple, regularly spaced, shallow rift basins and highs (Model W6).

3.1.2. Uplift and subsidence rates analysis

The evolution of surface topography can be regarded in terms of vertical-only uplift and subsidence or in terms of creation of accommodation space for water or sediments. Here we use the term *uplift/subsidence* to refer to the upward/downward vertical movement of the model surface. We use the term *accommodation space* to refer to created space below sea level, here an area in the 2D model, which is available for potential sediment accumulation. In Figure 5, we analyse the topography evolution (top left panels) of the four evolution-types described in the previous section: for Models D1, D5, W5 and W6, we compare the evolution of accommodation space (bottom right panels) with the horizontal and vertical velocities of the surface (top right and bottom left panels, respectively). Indeed, the creation of accommodation space does not only reflect the vertical velocity of the surface, but also the horizontal velocity of the surface. To illustrate the difference between creation of accommodation space and vertical movement, let us imagine a narrow and deep valley: if this valley is extended with only horizontal velocities perpendicular to the valley axis, then the valley widens and generates accommodation space, without the need of any downward-directed velocity. This distinction between creation of accommodation space and vertical surface motion is important in the following, when we analyse uplift and subsidence rates and relate these rates to the basin formation.

Figure 5: Top left panels: surface topography with time. Top right panels: surface horizontal velocity (x-direction) with time. Bottom left panels: surface vertical velocity with time. Bottom right panels: topography gradient with respect to time.

3.1.2.1 Analysis of Models with a Single, Narrow and Deep Rift Basin. Results of Model D1 (Figure 5a) are representative of Models D1, D2 and W1–W3. Model D1 shows a short phase of distributed extension between 0 and 0.5 My, as indicated by the low x-directed velocities along the entire model width (top right Figure 5a). Between 0.5 and 3 My, deformation localizes into a ca. 50 km-wide region in the model center, while the regions on either side move away from the model center as rigid blocks (see homogeneous velocities across them). During the last My of the simulation, deformation focuses into a 10 km-wide region, while the regions on either side behave as rigid blocks.

The vertical velocities across the model (bottom left panel of Figure 5a) also reflect the localization of deformation with time. Subsidence rate is relatively limited (less than 0.25 $mm \cdot y^{-1}$) during the phase of distributed deformation (until ca. 0.5 My). Then, it increases up to 4 $mm \cdot y^{-1}$ in the central region of active deformation. During the last 0.25 My of the simulation, the maximum subsidence rate decreases drastically to less than 0.5 $mm \cdot y^{-1}$. The region of maximum subsidence rate is framed by regions of maximum uplift rates (up to 1.5 $mm \cdot y^{-1}$). These regions of maximum uplift rate are located within the main rift basin and within an area of overall subsidence (compare bottom left, top left and bottom right panels of Figure 5a).

The evolution of the rate of accommodation space creation is comparable to that of the subsidence rate during the first 3 My of extension (compare bottom left, and bottom right panels of Figure 5a). The two plots start to significantly diverge when deformation localizes into the 10 km-wide region in the model center during the last My of the simulation (top right panel of Figure 5a): the domain recording subsidence (bottom left plot of Figure 5a) is much narrower than the domain recording overall subsidence (bottom right plot of Figure 5a). At this time, accommodation space creation is dominantly a result of subsidence only in the very center of the basin, while on either side accommodation space creation is mainly a consequence of the widening of an already deep basin (top panels of Figure 5a; see also the end of the first paragraph of section 3.1.2).

3.1.2.2 Analysis of Models with Three Rift Sub-basins. Results of Model D5 (Figure 5b) are representative of Models D3–D6. Model D5 shows a very short (less than 0.1 My) phase of distributed extension at the beginning of the simulation (top right panel of Figure 5b). Then, deformation focuses into a ca. 85 km-wide region in the model center, while the regions on either side are laterally displaced as rigid blocks. From ca. 5.3 My onward, the region of active deformation narrows rapidly into a 5 km-wide domain.

In contrast to Model D1, the bottom left plot of Figure 5b shows a complex pattern of vertical movements, where regions of uplift transitorily appear within the main rift basin. Until 4 My, the distribution and magnitudes of vertical velocities in the bottom left panel of Figure 5b are comparable with the subsidence and uplift rates displayed in the bottom right panel. During this time lag, both plots can be directly linked with the topographic evolution shown in the top left panel: the regions that move downward in the bottom left plot correspond to the different sub-basins of the top left plot, and the regions that move upward within the main rift basin correspond to the distal highs.

From ca. 5.3 My onward, subsidence starts to concentrate within the 5 km-wide domain of active deformation in the rift center (bottom left panel in Figure 5b). In contrast to Model D1, subsidence is maximal at the end of the necking phase in the rift center, where it reaches 1.5 $mm \cdot y^{-1}$. Uplift is also maximal at the end of the simulation in Model D5, where it reaches 1 $mm \cdot y^{-1}$ on either side of the axial rift zone. As in Model D1, the deviations between the vertical movements and the overall uplift/subsidence plots (bottom left and bottom right panels of Figure 5b) arise from the important horizontal displacement of already deep domains, which generates additional accommodation space.

3.1.2.3 Analysis of Models with Two Rift Sub-basins. Results of Model W5 (Figure 5c) are representative of Models W4 and W5. The evolution of horizontal velocities in Model W5 (top right panel in Figure 5c) is intermediate between that of Models D1 and D5. It starts with a very short phase of distributed extension (less than 0.1 My). Then, until ca. 5.3 My, deformation focuses within a ca. 60 km-wide region framed by two rigid blocks that move away from the model center.

From ca. 5.3 My onward, deformation focuses rapidly into a ca. 5 km-wide region in the

model center (top right panel in Figure 5c). Like in Model D5, subsidence is maximal in the rift center at this stage, where it reaches 1.5–1.75 $mm \cdot y^{-1}$ (bottom left panel in Figure 5c). Like in Model D5, the distribution and magnitudes of the vertical velocities are comparable with those of the subsidence and uplift rates until ca. 4.4 My (bottom left and bottom right panels of Figure 5c). During this time lag, both plots can be directly linked with the topographic evolution shown in the top left panel: the regions that move downward in the bottom left plot correspond to the different sub-basins of the top left plot, and the regions that move upward within the main rift basin correspond to the distal highs. The final deviation between the uplift/subsidence and accommodation space evolution plots (bottom left and bottom right panels of Figure 5c) is again a consequence of the horizontal displacement of deep domains that generates accommodation space.

3.1.2.4 Analysis of Model W6 with Multiple Rift Sub-basins. The horizontal velocity evolution of Model W6 is similar to that of Model D5 (Figure 5d). It starts with a brief phase of distributed extension followed by a 5 My long phase of deformation localized within a 80 km-wide region in the model center (top right panel in Figure 5d). From 5 My onward, deformation localizes rapidly into a 5 km-wide domain of active deformation framed by two rigid blocks that are displaced away from the rift center. Like in Models D5 and W5, subsidence is maximal in the rift center at this stage (bottom left panel in Figure 5d), where it reaches 1.5–2 $mm \cdot y^{-1}$.

The vertical velocity evolution is largely consistent with both the topographic and accommodation space evolutions during the first 6 My of the simulation (compare bottom and top left panels in Figure 5d). Then, like in Models D1, D5 and W5, the region recording increase in accommodation space becomes wider than the region characterized by downward-directed velocities. Here again, this divergence is a consequence of the widening of the existing central rift basin.

3.1.3. Accommodation Space and Emerged Area Evolution

Plotting the total accommodation space and emerged area created with time (Figures 6 and A.16) highlights that as much accommodation space as emerged area is created during the necking phase of every models. Three main trends stand out as a function of the crust rheology: (1) Models with a very strong crust (D1, D2, W1 and W2) show an initial (ca. 0.5 My) slight decrease in both accommodation space and emerged area. Then both increase extremely rapidly to values ranging

from 190 to 350 km^2 (Figures 6a–b and A.16a–b); (2) Models with a moderately strong crust (Models D3, D4, W3 and W4) show also an initial (ca. 1 My) slight decrease in both accommodation space and emerged area. Then, both increase progressively to values ranging from ca. 50 to 125 km^2 (Figures 6c–d and A.16a–b); (3) Models with a weak crust (Models D5, D6, W5 and W6) show also an initial (between 1.5 and 3 My) slight decrease in both accommodation space and emerged area. Then, both increase slightly to maximum 40 km^2. In the two models with the weakest crust (wet quartz crust Models D6 and W6), both accommodation space and emerged area remain less than their initial value. The reason is that the initial model topography (see Figure 2 and section 2) flattens during extension.

Figure 6: Evolution of the total accommodation space (blue curve) and total emerged area (red curve) with time along different models. Accommodation space and emerged area are corrected from the initial topography of the model, so that the graphs display how much additional accommodation space and emerged area are created with time.

3.1.4. Strain Rate and Stress Analysis

To understand which mechanical processes control the different evolutions reported in sections 3.1.2 and 3.1.3, we plot the second invariant of the strain rate tensor and the horizontal deviatoric stress for one model of each category (Models D1, D5, W5 and W6; Figure 7). In Models D1, D2, W1 and W2 the crust and mantle are largely mechanically coupled due to the very thin or inexistent weak ductile lower crust (Figure 2). The panels a–c of Figure 7 show that in Model D1 (like in Models D2 and W1–W3), the crust and upper mantle neck immediately and effectively as a single layer in the model center. The longer duration of the necking phase and the wider width of the rift basin of Model W3 compared to Models D1, D2, W1 and W2 can be explained by the significantly lower stress exponent of its crustal material (Bassi (1995); stress exponent $n = 3.1$ for the felsic granulite compared to $n = 4.7$ and 4.2 for the dry Maryland diabase and mafic granulite, respectively; see Table 1).

In Models D3–D6 and W4–W5 where the crust is moderately strong to weak, and thus decoupled from the upper mantle by a weak lower crust, a so-called ‘crustal keystone’ forms during the early stages of extension (Figures 7d and 7g). A keystone is a triangular-shaped piece of crust that remains relatively undeformed between two crustal scale faults/shear zones labelled ‘K’

in Figure 7 (Crosby & Crosby (1925); see also the 'H-Block' from Lavier & Manatschal (2006)). This keystone is subsequently split in two as deformation focuses to the model center, leaving one piece of 15–25 km thick continental crust (so-called 'continental lump' by Chenin et al., 2018) on either side of the rift center (Figures 7e–f and 7h–i). The splitting of the keystone forms a new sub-basin in the model center, which subsides rapidly during the last quarter of the simulation (Figures 4c, 4, 4f, A.15c–f and A.15i–k).

The topographic evolution of the Moho depends significantly of the mantle rheology: in models where the mantle is strong (Models D3–D6), the Moho remains deep (ca. 30 km) in the model center during the early stages of extension (see insets in Figures 7d and 7e). Consequently, the surface of the keystone records significant subsidence (300–800 m depth) after only 1–2 My of extension. In contrast, in Models W4–W5 where the mantle is weaker, the Moho starts rising in the model center as soon as extension begins (see insets in Figures 7g and 7h). Because the crust has not been significantly thinned at this stage yet, the surface of the keystone remains at shallow depth (200–300 m below zero).

Model W6 differs from the other models in that crustal deformation remains largely distributed within the upper crust until 5.5–6 My (Figures 7j and 7k). In Model W6, the combination between a small necking amplitude in the weak upper mantle and a thick decoupling lower crust prevents the formation of a keystone in the overlying upper crust (Figure 2). Instead, the lower crust is essentially thinned by pure shear and the four very shallow (less than 200 m deep) basins that are regularly spaced suggest the boudinage of the upper crust. Extension localizes eventually in the second basin to the right, where crustal necking is eventually achieved (Figure 7l).

The evolution of the horizontal deviatoric stress in Models D1 and D5 nicely illustrates the difference between effectively single-layer necking and two-layer necking of the lithosphere. During extension in Model D1, the stress is first positive (i.e. indicating extension) everywhere in the lithosphere (Figure 7a). With progressive extension the flexural rift shoulder uplift generates stresses that are negative (indicating compression) in the top region of the crust (Figures 7b and 7c). During extension in Model D5, stresses are also first positive everywhere in the lithosphere (Figure 7d). However, with progressive extension a significant neck only forms in the upper mantle, while the upper crust deforms in a distributed manner (Figures 7e and 7f). Consequently, the flexural uplift only occurs in the upper mantle and associated compressive stresses are

generated only in the upper region of the mantle lithosphere.

Figure 7: top panels: $\log_{10}$(second invariant of the strain rate tensor); bottom panels: horizontal deviatoric stress; the white line in each panel represents the Moho. The 'K' label marks the keystone block.

3.1.5. Thermal Evolution

Figures 8 and A.17 display the temperature at the end of the simulation and the relative cooling and heating compared to the initial stage. Figures 9 and A.18 show the surface heat flow with time along the model together with crustal thickness isopachs. These figures highlight that the weaker the crust, (1) the more important the asthenosphere upwelling; (2) the more offset between the initial lithosphere-asthenosphere boundary and the 1300 °C isotherm; (3) the larger the differential heating and cooling within the rift zone at the end of the simulation; and (4) the more complex the surface heat flow evolution.

Figure 8: Top panels: Difference between the initial and final temperature within the model at the end of the necking phase; temperature difference accounts for diffusion, production and advection of heat. The green lines represent top basement, Moho and initial lithosphere-asthenosphere boundary (the latter is visible on panels c–f only). Bottom panels: Model temperature at the end of the necking phase; the cyan lines represent top basement, Moho and the initial lithosphere–asthenosphere boundary; the dark blue lines represent the 250, 500, 750, 1000 and 1300 °C isotherms.

3.1.5.1 Temperature and Relative Heating/Cooling Distribution. In Models D1, D2, W1, W2 (strong crust), the amplitude of asthenosphere upwelling at the end of crustal necking is minor (less than 40 km in Model D1) compared to models with a weaker crust (more than 90 km in Model D6; see Figures 8 and A.17, bottom panels). In all models of Series W, the lithospheric mantle tends to delaminate and drip into the asthenosphere (Figures 8d, 8f and A.17g–l, bottom panels).

In all models, the temperature outside the central rift zone at the end of the simulation remains largely unchanged compared to the initial conditions (Figures 8 and A.17, top panels).

Within the rift zone, the bottom part of the crust is consistently heated in the very center of the model, while cooling occurs on either side. Cooling areas are located at the fault corridors controlling the rift shoulders in models with strongest crust (Models D1, D2, W1, W2; see Figure 7). They are located beneath the basins that frame the crustal keystone block in models with a weaker crust (Models D3-D6 and W4–W5). Models D4, D6 and W6 (and to a minor extent Models D3 and W3) show additionally significant cooling of the uppermost crust in the model center (i.e. not necessarily the rift center).

At the end of the simulation, the mantle beneath the rift center, which is usually former asthenospheric mantle, is consistently cooled compared to its initial temperature. Cooling ranges from 5–25 °C in models with strongest crust (D1, D2, W1 and W2) to > 100 °C in models with a moderately strong to weak crust (Models D3–D6 and W4–W6). Conversely, the mantle on either side of the asthenosphere upwelling is heated by 25–70 °C. Differential heating and cooling are generally higher in the models of Series D than in the equivalent models of Series W (Figures 8 and A.17, top panels).

In Models D3 to D6 (strong mantle, moderately strong to weak crust), one piece of mantle in the rift center keeps an elevated temperature with respect to its initial state (see arrows in insets in Figure A.17c–f). Yet, the smooth shape of the isotherm indicates the lack of a significant thermal anomaly. In Models W3–W6, two pieces of mantle keep an elevated temperature with respect to their initial state, one on either side of the rift center (see arrows in insets in Figure A.17i–l). These pieces corresponds to part(s) of the former 'upper mantle keystone', namely a block of subcontinental lithospheric mantle that remained largely undeformed between the two major shear zones that are associated with upper mantle necking. This mantle keystone was heated during the early stages of the simulation as a result of upper mantle necking, which juxtaposed parts of the uppermost mantle against deeper and hotter mantle. At the end of the simulation, the remnant of the initial mantle keystone is framed on its proximal side by the same shallow subcontinental mantle as initially, and on its distal side by deeper mantle that was upwelled during extension.

3.1.5.2 Surface Heat Flow. Figures 9 and A.18 show that surface heat flow is relatively homogeneous outside of the rift basin, with values of 50–70 $mW \cdot m^{-2}$. Within the main rift basin, surface heat flows of ca. 100 $mW \cdot m^{-2}$ are consistently observed from approximately half of the

necking duration onward. In models where one single rift basin forms (Models D1, D2 and W1–W3), the maximum heat flow is located in its center during the entire simulation (Figures 9a, 9b, 9d, A.18a–b and A.18g–i). In the other models, the highest heat flow is consistently recorded first in the two sub-basins that frame the crustal keystone. The highest heat flow remains in the outer sub-basins until the last quarter of the simulation, when the central sub-basin starts to deepen rapidly as the crust is efficiently thinned. From then onwards, the central sub-basin becomes the locus of highest heat flow (Figures 9c, 9e and 9f, A.18c–e and A.18j–k).

The crustal thickness isopachs of Figures 9 and A.18 highlight that surface heat flow is generally higher in regions of thinned crust. However, surface heat flow cannot be used to determine crustal thickness because: (1) to a given crustal thickness corresponds various heat flows depending on the crust and mantle rheology (Figures 9 and A.18); and (2) deviations between the location of highest heat flow and thinnest crust exist in most models and are more pronounced when the rheology of the lithosphere is weaker (see in particular Models D5 and W5 in Figure 9 and Model W6 in Figure A.18).

Figure 9: Surface heat flow with time along the different models. The contour lines represent crustal thickness isopachs: 15 km (black), 20 km (magenta) and 25 km (yellow). CC: continental crust.

3.2. Impact of Mantle Deformation Mechanism, Mantle Fertilization and Strain Softening

Figures 10, A.19, A.20 and A.21 display the results of Model Series D5+ where we tested the effect of the mantle creep mechanisms, mantle fertilization and strain softening. Figure 10a shows that topography at the end of the simulation is largely similar amongst the different models of Series D5+. The largest deviations with respect to Model D5 (black line) occur when either mantle fertilization (yellow line) or strain softening (violet and red lines) are modeled.

The necking duration remains also similar, differing by less than 1 My between the different models of Series D5+. The necking duration is slightly longer in Models D5+No diffusion creep, D5+Softening and D5+Softening CC (7.4 to 8.1 My compared to 7.3 My in Model D5) and shorter in the other models (minimum necking duration of 6.9 My in Model D5+No Peierls creep).

The minimum depth of the 500 °C isotherm at the end of the simulation is also largely similar amongst the different models of Series D5+, varying by less than 1 km with respect to Model D5 (Figure 10c). The minimum depth of the 1300 °C isotherm at the end of the simulation is more variable, ranging from 38 to 25 km compared to 32 km in Model D5 (Figure 10d). The 1300 °C isotherm is deepest at the end of the two simulations where diffusion creep is not modeled (36–37 km) and shallowest in the two simulations where strain softening is modeled (25–26 km). In Models D5+No diffusion & no Peierls creep (blue marker), the 500 °C isotherm is shallower by 0.5 km than in Model D5, while the 1300 °C isotherm is deeper by 5 km.

The maximum surface heat flow at the end of the simulation varies from less than 200 mW $\cdot$ m^{-2} in Models D5+Fertilization to 235 mW $\cdot$ m^{-2} in the two simulations where Peierls creep is not taken into account, while it is ca. 215 mW $\cdot$ m^{-2} in Model D5. However, Figure A.21 highlights that, except from Model D5+Softening CC, the distribution and intensity of surface heat flow is largely similar between Model D5 and the different models of Series D5+ during the three first quarters of the simulations (deviations < 10 mW $\cdot$ m^{-2}).

Figure 10: a) Surface topography at the end of the simulation of Model Series D5+; b) Necking duration of the different models; c) and d) Minimum depth of the 500 and 1300 °C isotherms at the end of the simulation; e) Maximum surface heat flow at the end of the simulation.

3.2.1. Impact of the Mantle Deformation Mechanism

Not considering either diffusion creep, or Peierls creep, or both decreases model asymmetry and slightly reduces the topographic height with respect to Model D5 (Figures 11a–b and A.19a–d). Rift shoulders reach a maximum height of 0.9 km and the continental lumps reach a maximum height of - 100 m in Models D5+No diffusion & no Peierls creep instead of 1 km and 0 m, respectively, in Model D5.

When Peierls creep is not considered, the mantle remains brittle-plastic to larger depths (45 km without Peierls creep included versus 35 km with Peierls creep for a dry olivine mantle; see Figure 2). One consequence is the slight reduction of the duration of extension required to achieve mantle necking. Consequently, crustal necking is also achieved earlier (6.9 versus 7.3 My; Figure 10b).

Diffusion creep provides lower effective viscosities at depth compared to dislocation creep (see Table 1 and Rybacki & Dresen (2000)). When diffusion creep is not considered, the duration of the necking phase is longer (7.4 versus 7.3 My; Figure 10b) and the 1300 °C isotherm is deeper at the end of the simulation (38 versus 32 km; Figure 10d). Consequently, the surface heat flow at the end of the simulation is lower compared to Model D5 (Figure A.21b)

The thermal architecture at the end of the necking phase is largely similar amongst the models with different mantle deformation mechanisms (Figures 12a–b and A.20a–d). In the two models without Peierls creep (Figures A.20c–d), there is no piece of mantle showing a relative heating with respect to initial temperature at the end of the simulation. Actually, a so-called 'mantle keystone' did form during the early stages of extension in both models, but because deformation was largely symmetrical, the mantle keystone was disintegrated during extension. Models without Peierls creep show a positive anomaly of more than 40 $mW \cdot m^{-2}$ in the surface heat flow (Figures A.21c–d) and a shallower 500 °C isotherm (Figure 10c) at the end of the simulation compared to Model D5.

Figure 11: Top panels: surface (magenta curve), top basement and Moho topography (black curves) at the end of the necking phase (i.e. when the crust is locally thinned to 10 km). The space between the magenta and top basement curves represents sediments. The horizontal blue line corresponds to the isobath 0 km. The 500 °C (and in panels c–e the 1300 °C) isotherms are plotted in red. Bottom panels: evolution of surface topography with time along the model. Strain soft.: Strain softening.

Figure 12: Top panels: Difference between the initial and final temperature within the model at the end of the necking phase; temperature difference accounts for diffusion, production and advection of heat. The green lines represent the Moho and the initial lithosphere-asthenosphere boundary. Middle panels: Model temperature at the end of the necking phase; the cyan lines represent the surface topography, top basement, Moho and the initial lithosphere–asthenosphere boundary; the dark blue lines represent the 250, 500, 750, 1000 and 1300 °C isotherms. Bottom panels: Difference in the surface heat flow compared to reference Model D5 with time along the model; the contour lines represent crustal thickness isopachs: 15 km (black), 20 km (magenta) and 25 km (yellow in panel a, blue in panels b–e). Strain soft.: Strain softening.

3.2.2. Impact of Mantle Fertilization

Model D5+Fertilization has an identical evolution as Model D5 until 5.4 My, which is the onset of mantle fertilization (compare panels a and c in Figure 11). From then onward, the decreased density of the fertilized mantle facilitates uplift and emersion above sea level in the region of the right-hand side continental lump. The emerged area is wider (up to 15 km) than in any other model.

Although we did not model the thermal effects of mantle fertilization (for instance the gain or loss of heat related to crystallization and melting or the heat transport due to melt migration), surface heat flow is higher by 15–20 $mW \cdot m^{-2}$ at the end of Model D5+Fertilization compared to Model D5 (Figure 12c). This increase in surface heat flow results from the facilitated upwelling of the fertilized mantle due to its decreased density (see shallower 500 °C isotherm at the end of the simulation in Figure 10c).

3.2.3. Impact of Strain Softening

Although the general spatio-temporal evolution remains similar amongst the simulations with and without strain softening, the topographic evolution of Models D5+Softening and D5+Softening CC is more symmetrical than that observed in Model D5 (Figures 11a, 11d and 11e). Surface topography is rougher and relief is more pronounced in models where strain softening is modeled due to the generation of prominent normal 'faults'/shear zones (Figure 13). These 'fault-like structures' are located where diffuse deformation zones occur in simulations without strain softening. The most external 'fault' on either side of the model (NF in Figures 13b and 13c and BF in Figures 13e–f and 13h–i) sits at the foot of the 'rift shoulder' (RS label in Figures 13a–b, 13e–f and 13h–i) and marks a sharp jump in the topographic height. These faults facilitate uplift. Indeed, rift shoulders reach more than 1.3 km high in models with strain softening, while they do not even reach 1 km in Model D5 (Figure 10a).

Like in Model D5, a crustal keystone forms in the model center of Models D5+Softening and D5+Softening CC (Figure 13). The keystone is thinned symmetrically in models with strain softening, conversely to Model D5. Consequently the model center remains more than 25 km-thick until 5 My in Models D5+Softening and D5+Softening CC, while it is already significantly thinned to less than 25 km at 4 My in Model D5. The thick keystone is transitorily emerged at ca.

5.5 My in the center of Model D5+Softening, while uplift close to the 0 km isobath occurs later (at ca. 6.5 My) on the right-hand side of the model (i.e. at the largest continental lump) in Model D5 (compare Figures 11a and 11d). The central part of the rift system is also uplifted in Model D5+Softening CC but it remains below 300 m depth.

In our study, strain softening is the process that has the most impact on the temperature and surface heat flow (compare Figures 12a, 12d and 12e). Although the general thermal architecture is comparable between Models D5, D5+Softening and D5+Softening CC, the 1300 $^{\circ}$ isotherm is shallower at the end of the simulation (Figure 10c) and many thermal heterogeneities appear on a local scale (Figures 12d and 12e). In both Models D5+Softening and D5+Softening CC, the well-developed 'faults' are sharp boundaries between regions of significant cooling and/or heating. The thermal heterogeneities within the mantle are more pronounced in Model D5+Softening compared to Model D5+Softening CC, however the impact on the surface heat flow is more pronounced in Model D5+Softening CC (compare top and lower panels of Figures 12d and 12e).

Figure 13: top panels: $\log_{10}$ (second invariant of the strain rate tensor); bottom panels: accumulated plastic strain (%); the white line in each panel represents the Moho. strain soft.: strain softening; K: keystone block; RS: rift shoulder; BF: border fault; NF: necking fault.

Figure 14: Synthetic view of the lithosphere architecture and main areas of cooling/heating with respect to initial temperature at the end of the necking stage for the four end-members behaviors deduced from our numerical model results; the lighter the red/blue the lower the heating/cooling. The graph above each panel shows the schematic topographic evolution at the main rift basin and adjacent continental lumps when applicable. nk: end of the necking phase. The duration of necking is largely controlled by the bulk extension rate (e.g. Chenin et al., 2018). For a bulk extension rate of 10^{-15} s^{-1} the necking phase lasts between ca. 3.5 and 8 My.

4. Discussion

4.1. Topographic evolution

In our simulations, we identify four types of rift system topographic and thermal evolutions

depending on there lithosphere rheology (field I, II, III and IV in Figure 14). The topographic evolution of models with a strong crust (Models D1, D2 and W1–W3; field I in Figure 14) is simple because it results from the necking of one single brittle-plastic layer that is comprised of the entire crust and the upper mantle lithosphere. This type of necking has been extensively described for instance by Buck (1991) and Bassi (1995).

The topographic evolution of models with a weak lower crust that decouples mechanically the brittle-plastic upper crust from the brittle-plastic upper mantle is more complex (fields II, III and IV in Figure 14). Such complexities are common in present-day numerical models but only rarely described in detail (e.g. Huismans & Beaumont, 2014; Van Wijk & Cloetingh, 2002). In our Models D3–D6 and W4–W6, we notice the formation of distal high(s) and sub-basins within the main rift basin at various stages of the necking phase (Figure A. 5). These sub-basins and highs form as a consequence of the asynchronous necking of first the upper mantle (strongest layer of the model; see Figure 2) and then the upper crust (second strongest layer of the model; see also Chenin et al. (2018, 2019)). Early necking of the upper mantle triggers the formation of a relatively undeformed crustal keystone (high) framed by two fault corridors (lows). As extension progresses, the asthenosphere starts upwelling beneath the center of the keystone and leads to its splitting in two. The splitting of the keystone forms a new sub-basin framed by two ridges (lumps) of thick continental crust (Models D3 and W3 in Figure 7; see also Chenin et al., 2018).

Mantle rheology impacts the topographic evolution of rift systems because it controls the depth of the upper mantle necking level (Braun & Beaumont, 1989; Kooi et al., 1992). As necking seeds around the strongest layer, which tends to remain horizontal (Weissel & Karner, 1989; Braun & Beaumont, 1989), initial subsidence is more pronounced in models where the mantle is strong to greater depth (compare graphs of fields II and III in Figure 14 and insets in Figures 7e and 7h). As the depth of the mantle necking level determines the magnitude of the Moho overdeepening, it also controls the amplitude of the subsequent flexural rebound when the necked layer tends to recover isostatic equilibrium. The amplitude of this rebound is more important when the magnitude of overdeepening is large and the flexural strength of the lithosphere is high (Weissel & Karner, 1989). In the case of a strong (dry olivine) mantle, the lithosphere has a high flexural strength and the Moho is largely over-deepened with respect to its isostatic position during upper mantle necking. As a consequence, the keystone subsides despite its high thickness (graph of field II in Figure 14). But once the upper mantle has been necked enough to locally loose most

of its strength, buoyancy forces bring the Moho upward, which explains the uplift of the two continental lumps (remnants of the former keystone) observed during late stages of the necking phase in Figure 5b. In contrast, when the upper mantle is weaker, the flexural strength of the mantle is lower and the upper mantle necking level is shallower. As a result, the Moho and the surface of the keystone remain shallower and the amplitude of the upper mantle isostatic rebound is lower (Figures 5c–d and graphs of fields III and IV in Figure 14).

Our models show that the creation of accommodation space during the necking phase of rifting is first mainly controlled by (vertical) subsidence. Then, towards the end of the necking phase, horizontal widening of the rift basin as a result of strong deformation localization becomes the dominant factor of accommodation space creation (see section 3.1.2).

Our results suggest that uplift and emersion are processes as common as is subsidence during the necking phase of rifting. Hence, subsidence is not the dominating topographic response to rifting, as implied by simple one-dimensional thinning models. Additional processes, such as flexure, crustal flow or lateral thermal diffusion, must be considered to predict both uplift and subsidence during rifting. The magnitude and spatio-temporal distribution of accommodation space creation and emersion are controlled by the rheology of the lithosphere (see section 3.1.3).

As already pointed out by Kaus et al. (2005) and Simon & Podladchikov (2008), mineral phase changes and/or mantle fertilization may lead to uplift of distal parts of rift systems during advanced stages of extension. Our modeling results suggest that density reduction related to mantle fertilization only can generate enough uplift to cause emersion of future distal regions comprised of relatively thick continental crust already during late stages of the necking phase. This uplift would be further increased when the heat related to melt advection and crystallization would be modeled. The effect of mantle fertilization is maximum in models where asthenosphere upwelling is fast compared to crustal thinning, that is in models with efficient mechanical decoupling between the crust and the mantle. In contrast, no mantle fertilization occurs during the necking phase of mechanically coupled models because the 1050 °C isotherm does not reach a depth of less than ca. 30 km during the simulation.

Our models with strain softening can be considered as end-members where the impact of this process is maximal (decrease of the internal angle of friction and cohesion from 30 ° to 5 ° and from 10 to 1 MPa, respectively, between 5% and 20% accumulated plastic strain). These models suggest that strain softening has a limited impact on the general architecture and evolution

of the modeled rift systems but significantly impacts the topography on a local scale. Strain softening facilitates differential vertical movements by enhancing localized deformation along fewer shear zones/'faults'. As a consequence, the topographic relief of our models with strain softening should be considered as maximal. However, results of models including strain softening must be interpreted with care because the numerical implementation is mesh-, and thus resolution-dependent. This means that the number of faults and their offset depend on the numerical resolution of the model.

The location of the major 'faults'/shear zones in models with strain softening is similar to that of the diffuse deformation zones in equivalent models without strain softening (Figure 13). Therefore, the zones of diffuse deformation of our models without strain softening can be interpreted as areas where major faults are likely to develop. Two sets of 'faults' are of particular interest: (1) we term 'necking faults' the outermost major faults that form during the early stages of extension (NF in the lower panels of Figures 13b and 13c). At this stage, the necking faults mark the boundary between the main rift basin and the rift shoulders (RS in the top panels of Figures 13b and 13c); (2) we term 'border faults' the outermost major faults in the subsequent frames (BF in the lower panels of Figures 13e–f and 13h–i). These 'faults' form later than the necking faults and mark the new boundary between the rift basin and its rift shoulders (RS in the top panels of Figures 13e–f and 13h–i). This implies that part of the initial rift shoulders may be integrated to the distal part of the margin as the necking phase progresses, as illustrated in Figures 11a, 11d and 11e. This model result has yet to be compared to field observations in order to assess the existence of such an evolution.

4.2. Thermal evolution

Our models show regions of differential cooling and heating in the lithosphere Figures 8 and A.17, while only cooling is predicted by DUT models (McKenzie, 1978). The thermal structure at the end of the simulation depends predominantly on the rheology of the crust. When the crust is strong and thus largely mechanically coupled to the upper mantle they neck rapidly as one single layer, and thus upwelling of the asthenosphere is only beginning when the necking phase is achieved. In contrast, when the crust is efficiently decoupled from the mantle by a weak lower crust, the earlier necking of the upper mantle triggers upwelling of the asthenosphere while the crust has not started thinning significantly yet. The asthenosphere keeps rising while the crust begins to neck, which accounts for the shallow 1300 °C isotherm and consequent high geothermal gradient at the end of the simulation. The same process explains the higher surface heat flow at the end of the simulation of models with a weak crust compared to models with a strong crust (Figures 9 and A.18).

Our models show consistently heating of the lower crust in the rift center and cooling of the crust on either side. Heating of the crust in the rift center is explained by the upwelling of hot (asthenospheric) mantle beneath it. Cooling of the crust on either side is a result of crustal thinning without significant underlying mantle thinning. Both the cooling and heating recorded in the mantle result from conductive heat exchange between the upwelling asthenosphere and the encompassing lithospheric mantle. In our models, cooling of the upwelling asthenosphere is enhanced because thermal convection below the lithosphere is not modeled (see section 2).

The amplitude of the relative heating/cooling within both the crust and the mantle is systematically less in models with a weak mantle (compare cartoon of field I with those of fields II, III and IV in Figure 14; see also Figure 8). Reasons are, on the one hand that the brittle-plastic uppermost part of the mantle is thinner in the weaker wet olivine mantle than in the dry olivine mantle (Figure 2). As a consequence, the necking instability is smaller in models with a wet olivine mantle, which triggers a wider and less pronounced upwelling of the asthenosphere compared to models with a dry olivine mantle. On the other hand, the weaker wet olivine mantle is more sensitive to Rayleigh–Taylor instabilities, which result in the delamination of the lowermost part of the lithospheric mantle into the asthenosphere (Figures A.17g–l). Consequently, part of the thermal exchanges occur at depth to the detriment of the shallower part of the lithosphere.

Intense strain softening (internal angle of friction and cohesion reduced from 30 ° to 5 °

and from 10 to 1 MPa, respectively) has a significant impact on the thermal evolution of our models, although we did not associate any modification of the thermal conductivity (or any other thermal parameter) to the formation of faults. In our models, we observe that faults are associated with sharp changes in the relative cooling/heating, especially within the crust. One reason for this is the concentration of shear heating along the fewer and more localized faults, which generates significant heating compared to models devoid of strain softening. As in natural rift systems faults are regions of increased permeability, and thus of efficient fluid circulation and heat transport (e.g. Pinto et al., 2015; Incerpi et al., 2019), we suggest that integrating major faults into basin modeling is necessary to obtain a reliable understanding of the thermal evolution of a rift system.

In models where the crust and the mantle are mechanically decoupled, the asthenosphere reaches a depth of less than 40 km at the end of the necking phase. Partial melting of the asthenosphere may be likely under such conditions in natural rift systems. As melt percolation may substantially modify the thermal state of rift systems, a careful quantification of the gain/loss of heat related to magma crystallization/melting processes and of heat transfers due to melt advection should be undertaken in such cases. A first step was made by van Wijk et al. (2001), who estimated the amount of melt produced by decompression melting for comparable model settings. They show that volumes of several hundreds of km^3 may be generated during late syn-rift stages (consistently after 15 My). In our decoupled models, we would expect the onset of melt generation from 5–6 My of extension already in models with a relatively weak crust.

4.3. Synthesis: Primary Control on Topographic and Thermal Evolution of Rift Systems

Our results show that the rheology of the lithosphere, in particular the efficiency of mechanical coupling between the crust and the mantle, is the dominant parameter controlling both the topographic and thermal evolution of rift systems (Figure 14). Mechanical decoupling between the crust and the mantle favors complex topographic evolution during extension and high geothermal gradients at the end of the necking phase. When studying continental rifting, it is therefore of primary importance to determine the distribution of strong versus weak (decoupling) layers within the lithosphere, which is essentially controlled by: (1) the composition of the crust and mantle; (2) the crustal thickness; and (3) the geothermal gradient (Kusznir & Park, 1987; Burov & Diament, 1995). At present, most studies assume that lithospheric strength is essentially

controlled by dislocation creep, sometimes also by diffusion and Peierls creep flow laws of monomineralic materials derived from experimental data (e.g. Kirby, 1980; Kohlstedt et al., 1995; Kusznir & Park, 1987; Tesauro et al., 2012). These studies predict that, under a low to moderate geothermal gradient, the strongest layer of the lithosphere is the uppermost mantle, which is consistent with the persistence of mountain ranges on geological time scales (Burov & Watts, 2006). However, Maggi et al. (2000) noticed that lithospheric seismicity is largely limited to crustal layers, while the upper mantle is essentially aseismic. They concluded that, at least in some places, the lower crust is stronger than the upper mantle.

4.4. Geological outlooks

The necking stage is a transient phase of rift evolution. Because it is out of equilibrium both from a thermal and isostatic perspective, it is not preserved in the final margin architecture. The best insights we have on the necking stage of rifting arise from the sedimentary record and erosional unconformities observed at present-day and fossils rifted margins. However, due to the lack of a continuous geological record by the sediments and/or precise dating of sedimentary deposits in deep-water margins, a comprehensive comparison between the topographic evolution of our models and natural rifted margins is currently impossible. Our models provide a first quantification of the possible topographic and thermal evolutions during the necking phase, which need to be compared to the evolution of calibrated natural examples. This step is not straightforward because seismically well-imaged rifted margins of which the distal domain is calibrated with drill holes are rare or data are proprietary. At this stage, we are only able to discuss primary similarities between our models and natural rift systems.

Models where the crust and the mantle are mechanically decoupled predict a complex topographic evolution and both heating and cooling events during the necking phase, consistent with growing evidence from both field studies and drill hole data. Indeed, the existence of local erosional features at distal rifted margins and/or the record of a heating event at the base of the crust during rifting suggest that rift systems do neither necessarily experience immediate and progressive subsidence (Esedo et al., 2012), nor only progressive post-extensional cooling (e.g. Smye & Stockli, 2014; Hart et al., 2017), conversely to what is predicted by the DUT model (McKenzie, 1978).

Models W4 and W5 predict the keystone to remain less than 200–300 m deep during

approximately half of the necking phase (Figure A.15). This result can be compared to the evolution of the Iberian margin, whose distal domain appears to have remained at shallow water depth (within the photic zone) during early stages of the necking phase in Tithonian–Berriasian time (ca. 145 Ma; Boillot et al., 1988; Mohn et al., 2014, compare Figure 1b and graph III in Figure 14). This hypothesis remains yet to be tested against calibrated stratigraphic data.

Models D6, D5+Fertilization and D5+Softening can account for the existence of syn-rift erosional unconformities at distal parts of rift systems since part of their initial keystone becomes transitorily emerged after an initial phase of subsidence (Figures 11c and 11d). This evolution can be compared with that of the Briançonnais unit during the Early Jurassic necking phase of the former Alpine Tethys. The Briançonnais unit, which is characterized by Early Jurassic karsts (e.g. Claudel & Dumont, 1999), is interpreted to have initially formed as a keystone and have become part of the distal European margin at the time of breakup (Lavier & Manatschal, 2006).

The evolution of Models D6, D5+Fertilization and D5+Softening can also be compared with that of the outer Campos Basin hinge offshore the Brazilian margin, where a few tens of kilometers wide erosional unconformity was mapped over 120 km along strike (e.g. Lewis et al., 2014). The fact that the eroded region is linear, of relatively constant width and sub-parallel to the coastline suggests that its origin is structural/tectonic rather than thermal. Lewis et al. (2014) interpreted the unconformity to be syn-rift. One of the scenarios for its formation was that part of the outer hinge experienced transitory uplift and emersion during the Aptian, after which the entire outer hinge subsided. They rejected this scenario because they could not find a geological process accounting for ca. 1 km of local uplift followed by 2–3 km of subsidence in the span of 13 My. Assuming Models D5+Fertilization and D5+Softening explain this behavior, the transitory uplift of the outer hinge would be related to the isostatic adjustment of a former keystone after the necking of the upper mantle.

Due to the lack of access to lower crustal levels, the deep thermal evolution of rift basins and hyperextended rift systems is poorly known. The only direct information come from fossil hyperextended rift systems now exposed in the Pyrenean and the Alpine orogens in Western Europe. Thermochronological data from these systems indicate intense heating events during the necking phase of rifting (Smye & Stockli, 2014; Seymour et al., 2016; Hart et al., 2017). Based on the high geothermal gradients at the end of the necking phase, we suggest that the Pyrenean and Alpine rift systems developed within a lithosphere where the crust and the mantle were

mechanically decoupled, which allowed for asynchronous necking of first the upper mantle, and then the crust. In the Pyrenees, the widespread occurrence of a pre-rift salt further promoted intra-crustal mechanical decoupling during rifting (Duretz et al., 2020).

According to our model results, surface heat flow could be used as a proxy to localize regions of thinned crust. In particular, two regions of higher-than-average surface heat flow separated by a few tens of kilometers may highlight the boundaries of a crustal keystone prior to significant crustal thinning.

5. Conclusion

We performed a systematic analysis with a high-resolution thermo-mechanical model to quantify the impact of lithosphere rheology on the topographic and thermal evolutions during the necking phase of extensional systems (i.e. until the crust is thinned to 10 km). Our results confirm that the rheology of the lithosphere has a major control on the topography evolution. We argue that this control arises from: (1) the efficiency of the mechanical decoupling between the crust and the mantle, and thus the delay between crust and mantle necking; (2) the depth of the necking level(s), and thus the amplitude of the initial subsidence and subsequent isostatic rebound; and (3) the flexural strength of the lithosphere, and thus the regionality and efficiency of isostatic compensation. When the mantle is strong and the crust weak to moderately strong, extension of the lithosphere results in the formation of several highs and sub-basins within the main rift basin. This architecture differs significantly from the traditional view that, in the absence of several weak inherited structures, extension of the lithosphere produces one single basin that subsides progressively. Adjacent highs and lows are usually characterized by positive and negative vertical velocities, respectively. These differential uplift and subsidence movements can occur over a region of a few tens of kilometers only.

The creation of accommodation space is primarily controlled by (vertical) subsidence during the early stages of rifting. By the end of the necking phase, creation of accommodation space is largely caused by horizontal extension as a result of intense deformation localization at the rift center. Our models show that a comparable amount of accommodation space and emerged area is created during the necking phase of rifting. We conclude that during the necking phase of rifting, uplift and emersion are as common processes as is subsidence. Hence, subsidence is not the dominating topographic response to rifting, as is implied by simple thinning models. The rheology

of the lithosphere controls the magnitude and spatiotemporal distribution of uplift and emersion during necking, which we quantified in detail in our study.

The efficiency of mechanical decoupling between the crust and mantle controls also the geothermal gradient at the rift center at the end of the necking phase. When the crust is mechanically decoupled from the upper mantle, earlier necking of the upper mantle triggers the onset of asthenosphere upwelling beneath an largely un-thinned crust, which results in a particularly high geothermal gradient in the rift center. In this case, partial melting and consequent fertilization of the subcontinental lithospheric mantle by melt impregnation are likely and may lead to increased uplift of future distal parts of the rifted margins.

Acknowledgment

This Research was conducted in the framework of the Margins 5 consortium, which involves BP, BHP, CNOOC UK Limited, Conocophillips, Econor, Ecopetrol, HESS, Petrobras, Repsol, Shell, Total, ION, CGG. We thank Nick Kusznir for helpful discussions on this manuscript.

Declaration of interests

The authors declare that they have no known competing financial interests or personal relationships that could have appeared to influence the work reported in this paper.

References

Artemjev, M. E., & Artyushkov, E. V. (1971). Structure and Isostasy of the Baikal Rift and the mechanism of rifting. *Journal of Geophysical Research, 76,* 1197–1211.

Ball, P., Eagles, G., Ebinger, C., McClay, K., & Totterdell, J. (2013). The spatial and temporal evolution of strain during the separation of Australia and Antarctica. *Geochemistry, Geophysics, Geosystems, 14,* 2771–2799. URL: http://doi.wiley.com/10.1002/ggge.20160. doi: 10.1002/ggge.20160.

Bassi, G. (1991). Factors controlling the style of continental rifting: insights from numerical modelling. *Earth and Planetary Science Letters, 105,* 430–452. doi: 10.1016/0012-821X(91)90183-I.

Bassi, G. (1995). Relative importance of strain rate and rheology for the mode of continental

extension. *Geophysical Journal International, 122,* 195–210.

Beltrando, M., Stockli, D. F., Decarlis, A., & Manatschal, G. (2015). A crustal-scale view at rift localization along the fossil Adriatic margin of the Alpine Tethys preserved in NW Italy. *Tectonics, 34,* 1927–1951. URL: http://doi.wiley.com/10.1002/2015TC003973. doi: 10.1002/2015TC003973.

Boillot, G., Girardeau, J., & Kornprobst, J. (1988). Rifting of the Galicia margin: crustal thinning and emplacement of mantle rocks on the seafloor. In G. Boillot, & E. L. Winterer (Eds.), *Proceeding of the Ocean Drilling Program, Scientific Results* chapter 41. (pp. 733–740). volume 103.

Bourbon, M. (1980). *Evolution d'un secteur de la marge nord-téthysienne en milieu pélagique: la zone briançonnaise près de Briançon entre le début du Malm et l'Eocène inférieur*. Ph.D. thesis Université Louis Pasteur.

Braun, J., & Beaumont, C. (1989). A physical explanation of the relation between flank uplifts and the breakup unconformity at rifted continental margins. *Geology, 17,* 760–764. doi: 10.1130/0091-7613(1989)017<0760:APEOTR>2.3.CO.

Buck, W. R. (1991). Modes of continental lithospheric extension. *Journal of Geophysical Research, 96,* 20,161–20,178.

Burov, E., & Poliakov, A. (2001). Erosion and rheology controls on synrift and postrift evolution: Verifying old and new ideas using a fully coupled numerical model. *Journal of Geophysical Research: Solid Earth, 106,* 16461–16481.

Burov, E., & Poliakov, A. (2003). Erosional forcing of basin dynamics: new aspects of syn- and post-rift evolution. *Geological Society, London, Special Publications, 212,* 209–223. URL: http://sp.lyellcollection.org/lookup/doi/10.1144/GSL.SP.2003.212.01.14. doi: 10.1144/GSL.SP.2003.212.01.14.

Burov, E. B., & Diament, M. (1995). The effective elastic thickness (Te) of continental lithosphere: What does it really mean? *Journal of Geophysical Research, 100,* 3905–3927.

Burov, E. B., & Watts, A. B. (2006). The long-term strength of continental lithosphere: ?Äújelly sandwich?Äù or ?Äúcrème brûlée?Äù? *GSA Today, 16,* 4–10. doi: 10.1130/1052-5173(2006)016<4:TLTSOC>2.0.CO;2 4 JaNuaRy.

Campbell, I. H. (2005). Large Igneous Provinces and the Mantle Plume Hypothesis. *Elements, 1,*

265–269. URL: https://pubs.geoscienceworld.org/elements/article/1/5/265-269/137587. doi: 10.2113/gselements.1.5.265.

Chenin, P., Manatschal, G., Decarlis, A., Schmalholz, S. M., Duretz, T., & Beltrando, M. (2019). Emersion of distal domains in advanced stages of continental rifting explained by asynchronous crust and mantle necking. *Geochemistry, Geophysics, Geosystems,*. doi: 10.1029/2019GC008357.

Chenin, P., Manatschal, G., Picazo, S., Müntener, O., Karner, G. D., Johnson, C., & Ulrich, M. (2017). Influence of the architecture of magma-poor hyperextended rifted margins on orogens produced by the closure of narrow versus wide oceans. *Geosphere, 13,* 1–18. doi: 10.1130/GES01363.1.

Chenin, P., Schmalholz, S. M., Manatschal, G., & Karner, G. D. (2018). Necking of the lithosphere : a reappraisal of basic concepts with thermo-mechanical numerical modeling. *Journal of Geophysical Research : Solid Earth, 123*, 5279–5299. doi: 10.1029/2017JB014155.

Claudel, M. E., & Dumont, T. (1999). A record of multistage continental break-up on the Briançonnais marginal plateau (Western Alps): Early and Middle-Late Jurassic rifting. *Eclogae Geologicae Helvetiae*, *92*, 45–61.

Cloetingh, S., Van Wees, J., Van der Beek, P., & Spadini, G. (1995). Role of pre-rift rheology in kinematics of extensional basin formation: constraints from thermomechanical models of mediterranean and intracratonic basins. *Marine and Petroleum Geology, 12*, 793–807.

Crosby, W., & Crosby, J. B. (1925). Keystone faults. *Bulletin of the Geological Society of America, 36*, 623–640.

Driscoll, N. W., & Karner, G. D. (1998). Lower crustal extension accross the Northern Carnarvon basin, Australia: Evidence for an eastward dipping detachment. *Journal of Geophysical Research, 103*, 4975–4991.

Duretz, T., Asti, R., Lagabrielle, Y., Brun, J.-P., Jourdon, A., Clerc, C., & Corre, B. (2020). Numerical modelling of cretaceous pyrenean rifting: The interaction between mantle exhumation and syn-rift salt tectonics. *Basin Research,*. URL: https://onlinelibrary.wiley.com/doi/abs/10.1111/bre.12389. doi: 10.1111/bre.12389. arXiv:https://onlinelibrary.wiley.com/doi/pdf/10.1111/bre.1

2389.

Duretz, T., May, D., & Yamato, P. (2016a). A free surface capturing discretization for the staggered grid finite difference scheme. *Geophysical Journal International, 204,* 1518–1530. URL: https://academic.oup.com/gji/article-lookup/doi/10.1093/gji/ggv526. doi: 10.1093/gji/ggv526.

Duretz, T., Petri, B., Mohn, G., Schmalholz, S. M., Schenker, F. L., & Müntener, O. (2016b). The importance of structural softening for the evolution and architecture of passive margins. *Scientific reports, 6,* 38704. URL: http://www.ncbi.nlm.nih.gov/pubmed/27929057 http://www.pubmedcentral.nih.gov/articlerender.fcgi?artid=PMC5144128. doi: 10.1038/srep38704.

Esedo, R., van Wijk, J., Coblentz, D., & Meyer, R. (2012). Uplift prior to continental breakup: Indication for removal of mantle lithosphere? *Geosphere, 8,* 1078–1085. URL: http://pubs.geoscienceworld.org/geosphere/article/8/5/1078/132546/Uplift-prior-to-continental-breakup-Indication-for. doi: 10.1130/GES00748.1.

Evans, B., & Goetze, C. (1979). The temperature variation of hardness of olivine and its implication for polycrystalline yield stress. *Journal of Geophysical Research: Solid Earth, 84,* 5505–5524.

Gartrell, A. P. (2001). Crustal rheology and its effect on rift basin styles. In H. A. Koyi, & N. S. Mancktelow (Eds.), *Tectonic Modeling: A Volume in Honor of Hans Ramberg* (pp. 221–234). Geological Society of America Memoir 193.

Hart, N. R., Stockli, D. F., Lavier, L. L., & Hayman, N. W. (2017). Thermal evolution of a hyperextended rift basin, Mauléon Basin, western Pyrenees. *Tectonics, 36,* 1103–1128.

Haupert, I., Manatschal, G., Decarlis, A., & Unternehr, P. (2016). Upper-plate magma-poor rifted margins: stratigraphic architecture and structural evolution. *Marine and Petroleum Geology, 69,* 241–261. URL: http://dx.doi.org/10.1016/j.marpetgeo.2015.10.020. doi: 10.1016/j.marpetgeo.2015.10.020.

Hendrie, D., Kusznir, N., & Hunter, R. (1993). Jurassic extension estimates for the North Sea

?triple junction' from flexural backstripping: implications for decompression melting models. *Earth and Planetary Science Letters, 116,* 113–127. URL: https://www.sciencedirect.com/science/article/pii/0012821X9390048E. doi: 10.1016/0012-821X(93)90048-E.

Hirth, G., & Kohlstedt, D. (2003). Rheology of the upper mantle and the mantle wedge: A view from the experimentalists. In J. Eiler (Ed.), *Inside the subduction Factory*.

Huismans, R., & Beaumont, C. (2011). Depth-dependent extension, two-stage breakup and cratonic underplating at rifted margins. *Nature, 473,* 74–78. URL: http://www.ncbi.nlm.nih.gov/pubmed/21544144. doi: 10.1038/nature09988.

Huismans, R. S., & Beaumont, C. (2007). Roles of lithospheric strain softening and heterogeneity in determining the geometry of rifts and continental margins. In G. D. Karner, G. Manatschal, & L. M. Pinhiero (Eds.), *Imaging, Mapping and Modelling Continental Lithosphere Extension and Breakup* (pp. 107–134). Geological Society, London, Special Publications, 282.

Huismans, R. S., & Beaumont, C. (2014). Rifted continental margins: The case for depth-dependent extension. *Earth and Planetary Science Letters, 407,* 148–162. URL: http://dx.doi.org/10.1016/j.epsl.2014.09.032. doi: 10.1016/j.epsl.2014.09.032.

Incerpi, N., Martire, L., Manatschal, G., Bernasconi, S. M., Gerdes, A., Czuppon, G., Palcsu, L., Karner, G. D., Johnson, C. A., & Figueredo, P. H. (2019). Hydrothermal fluid flow associated to the extensional evolution of the Adriatic rifted margin: Insights from the pre?to post?rift sedimentary sequence (SE Switzerland, N ITALY). *Basin Research,* (pp. 1–25). doi: 10.1111/bre.12370.

Kameyama, M., Yuen, D. A., & Karato, S.-I. (1999). Thermal-mechanical effects of low-temperature plasticity (the peierls mechanism) on the deformation of a viscoelastic shear zone. *Earth and Planetary Science Letters, 168,* 159–172.

Kaus, B. J., Connolly, J. A., Podladchikov, Y. Y., & Schmalholz, S. M. (2005). Effect of mineral phase transitions on sedimentary basin subsidence and uplift. *Earth and Planetary Science Letters, 233,* 213–228. URL: http://linkinghub.elsevier.com/retrieve/pii/S0012821X050008

16 http://www.sciencedirect.com/science/article/pii/S0012821X05000816. doi: 10.1016/j.epsl.2005.01.032.

Kirby, S. H. (1980). Tectonic stresses in the lithosphere: constraints provided by the experimental deformation of rocks. *Journal of Geophysical Research, 85,* 6353–6363. doi: 10.1029/JB085iB11p06353.

Kohlstedt, D. L., Evans, B., & Mackwell, S. J. (1995). Strength of the lithosphere: Constraints imposed by laboratory experiments. doi: 10.1029/95JB01460.

Kooi, H., Cloetingh, S., & Burrus, J. (1992). Lithospheric necking and regional isostasy at extensional basins 1. Subsidence and gravity modeling with an application to the Gulf of Lions Margin (SE France). *Journal of Geophysical Research, 97,* 17553. doi: 10.1029/92JB01377.

Kusznir, N. J., & Karner, G. D. (2007). Continental lithospheric thinning and breakup in response to upwelling divergent mantle flow: application to the Woodlark, Newfoundland and Iberia margins. *Geological Society, London, Special Publications, 282,* 389–419. doi: 10.1144/SP282.16.

Kusznir, N. J., & Park, R. G. (1987). The extensional strength of the continental lithosphere: its dependence on geothermal gradient, and crustal composition and thickness. *Geological Society, London, Special Publications, 28,* 35–52. URL: http://sp.lyellcollection.org/content/28/1/35.short. doi: 10.1144/GSL.SP.1987.028.01.04.

Lavier, L. L., & Manatschal, G. (2006). A mechanism to thin the continental lithosphere at magma-poor margins. *Nature, 440,* 324–328. URL: http://www.ncbi.nlm.nih.gov/pubmed/16541070. doi: 10.1038/nature04608.

Lemoine, M., Tricart, P., & Boillot, G. (1987). Ultramafic and gabbroic ocean floor of the Ligurian Tethys (Alps, Corsica, Apennines): In search of a genetic imodel. *Geology, 15,* 622–625. URL: http://geology.gsapubs.org/content/15/7/622.short. doi: 10.1130/0091-7613(1987)15.

Lewis, D. S., Ross, E., & Leander, M. (2014). New insights into late synrift subsidence from detailed well ties and seismic mapping, Campos Basin, Brazil. In J. Pindell, B. Horn, N.

Rosen, P. Weimer, M. Dinkleman, A. Lowrie, R. Fillon, J. Granath, & L. Kennan (Eds.), *Sedimentary basins: origin, depositional histories and petroleum systems* (pp. 98–115). Houston : SEPM Society for Sedimentary Geology.

Lin, A., Watts, A., & Hesselbo, S. (2003). Cenozoic stratigraphy and subsidence history of the south china seamargin in the taiwan region. *Basin Research, 15,* 453–478.

Mackwell, S. J., Zimmerman, M. E., & Kohlstedt, D. L. (1998). High-temperature deformation of dry diabase with application to tectonics on Venus. *Journal of Geophysical Research: Solid Earth, 103,* 975–984. URL: http://doi.wiley.com/10.1029/97JB02671. doi: 10.1029/97JB02671.

Maggi, A., Jackson, J. A., Priestley, K., & Baker, C. (2000). A re-assessment of focal depth distributions in southern Iran, the Tien Shan and northern India: do earthquakes really occur in the continental mantle? *Geophysical Journal International, 143,* 629–661. URL: http://gji.oxfordjournals.org/content/143/3/629.abstract. doi: 10.1046/j.1365-246X.2000.00264.x.

McCarthy, A., & Müntener, O. (2015). Ancient depletion and mantle heterogeneity: Revisiting the Permian-Jurassic paradox of Alpine peridotites. *Geology, 43,* 255–258. URL: http://geology.gsapubs.org/cgi/doi/10.1130/G36340.1. doi: 10.1130/G36340.1.

McKenzie, D. (1978). Some remarks on the development of sedimentary basins. *Earth and Planetary Science Letters, 40,* 25–32. URL: http://linkinghub.elsevier.com/retrieve/pii/0012821X78900717. doi: 10.1016/0012-821X(78)90071-7.

Mohn, G., Karner, G., Manatschal, G., & Johnson, C. (2014). Structural and stratigraphic evolution of the Iberia and Newfoundland hyper-extended rifted margins : A quantitative modeling approach. *Geological Society London Special Publication, 16,* 9156. doi: 10.1144/SP413.9.

Mohn, G., Manatschal, G., Beltrando, M., Masini, E., & Kusznir, N. (2012). Necking of continental crust in magma-poor rifted margins: Evidence from the fossil Alpine Tethys margins. *Tectonics, 31,* TC1012. URL: http://doi.wiley.com/10.1029/2011TC002961. doi: 10.1029/2011TC002961.

Müntener, O., Hermann, R. G., & Trommsdorff, V. (2000). Cooling History and Exhumation of Lower- Crustal Granulite and Upper Mantle (Malenco, Eastern Central Alps). *Journal of Petrology, 41*, 175–200.

Müntener, O., Manatschal, G., Desmurs, L., & Pettke, T. (2010). Plagioclase peridotites in ocean-continent transitions: Refertilized mantle domains generated by melt stagnation in the shallow mantle lithosphere. *Journal of Petrology, 51*, 255–294. URL: http://www.petrology.oxfordjournals.org/cgi/doi/10.1093/petrology/egp087. doi: 10.1093/petrology/egp087.

Petri, B., Duretz, T., Mohn, G., Schmalholz, S. M., Karner, G. D., & Müntener, O. (2019). Thinning mechanisms of heterogeneous continental lithosphere. *Earth and Planetary Science Letters, 512*, 147–162.

Pinto, V. H. G., Manatschal, G., Karpoff, A. M., & Viana, A. (2015). Tracing mantle-reacted fluids in magma-poor rifted margins: The example of Alpine Tethyan rifted margins. *Geochemistry, Geophysics, Geosystems, 16*, 3271–3308. URL: http://doi.wiley.com/10.1002/2015GC005830. doi: 10.1002/2015GC005830.

Popov, A. A., & Sobolev, S. V. (2008). SLIM3D: A tool for three-dimensional thermomechanical modeling of lithospheric deformation with elasto-visco-plastic rheology. *Physics of the Earth and Planetary Interiors, 171*, 55–75. URL: http://www.sciencedirect.com/science/article/pii/S003192010800054X. doi: 10.1016/j.pepi.2008.03.007.

Ranalli, G. (1995). *Rheology of the Earth*. Chapman & Hall. URL: https://books.google.fr/books?hl=fr{&}lr={&}id=cBezMivXS2YC{&}oi=fnd{&}pg=PP13{&}dq=Ranalli+1995{&}ots=_JJOB4zMaQ{&}sig=9dvPoO8PX0fBSaHgL0hU68CWyyQ#v=onepage&q=Ranalli 1995{&}f=false.

Ranalli, G. (1997). Rheology of the lithosphere in space and time. *Geological Society, London, Special Publications, 121*, 19–37. URL: http://sp.lyellcollection.org/content/121/1/19.abstract. doi: 10.1144/gsl.sp.1997.121.01.02.

Reston, T. J., Pennel, J., Stubenrauch, A., Walker, I., & Perez-Gussinye, M. (2001). Detachment

faulting, mantle serpentinization and serpentinite-mud volcanism beneath the Porcupine Basin, southwest of Ireland. *Geology*, *29*, 587–590.

Ribes, C., Manatschal, G., Ghienne, J.-F., Karner, G. D., Johnson, C. A., Figueredo, P. H., Incerpi, N., & Epin, M.-e. (2019). The syn-rift stratigraphic record across a fossil hyper-extended rifted margin: the example of the northwestern Adriatic margin exposed in the Central Alps. *International Journal of Earth Sciences,*. doi: DOI: 10.1007/s00531-019-01750-6.

Roberts, A. M., Lundin, E. R., & Kusznir, N. J. (1997). Subsidence of the Vøring Basin and the influence of the Atlantic continental margin. *Journal of the Geological Society*, *154*, 551–557. URL: http://jgs.lyellcollection.org/lookup/doi/10.1144/gsjgs.154.3.0551. doi: 10.1144/gsjgs.154.3.0551.

Royden, L., & Keen, C. (1980). Rifting process and thermal evolution of the continental margin of eastern canada determined from subsidence curves. *Earth and Planetary Science Letters*, *51*, 343–361.

Rybacki, E., & Dresen, G. (2000). Dislocation and diffusion creep of synthetic anorthite aggregates. *Journal of Geophysical Research: Solid Earth*, *105*, 26017–26036. URL: http://doi.wiley.com/10.1029/2000JB900223. doi: 10.1029/2000JB900223.

Rybacki, E., & Dresen, G. (2004). Deformation mechanism maps for feldspar rocks. *Tectonophysics*, *382*, 173–187. doi: 10.1016/j.tecto.2004.01.006.

Seymour, N. M., Stockli, D. F., Beltrando, M., & Smye, A. J. (2016). Tracing the thermal evolution of the Corsican lower crust during Tethyan rifting. *Tectonics*, *35*, 2439–2466. doi: 10.1002/2016TC004178.

Simon, N. S., & Podladchikov, Y. Y. (2008). The effect of mantle composition on density in the extending lithosphere. *Earth and Planetary Science Letters*, *272*, 148–157. URL: http://www.sciencedirect.com/science/article/pii/S0012821X08002744. doi: 10.1016/j.epsl.2008.04.027.

Smye, A. J., & Stockli, D. F. (2014). Rutile U-Pb age depth profiling: A continuous record of lithospheric thermal evolution. *Earth and Planetary Science Letters*, *408*, 171–182. URL: http://dx.doi.org/10.1016/j.epsl.2014.10.013. doi:

10.1016/j.epsl.2014.10.013.

Sutra, E., Manatschal, G., Mohn, G., & Unternehr, P. (2013). Quantification and restoration of extensional deformation along the Western Iberia and Newfoundland rifted margins. *Geochemistry, Geophysics, Geosystems, 14,* 2575–2597. URL: http://doi.wiley.com/10.1002/ggge.20135. doi: 10.1002/ggge.20135.

Svartman Dias, A. E., Lavier, L. L., & Hayman, N. W. (2015). Conjugate rifted margins width and asymmetry: The interplay between lithospheric strength and thermomechanical processes. *Journal of Geophysical Research: Solid Earth, 120,* 8672–8720.

Tesauro, M., Kaban, M. K., & Cloetingh, S. A. (2012). Global strength and elastic thickness of the lithosphere. *Global and Planetary Change, 90-91,* 51–57. URL: https://www.sciencedirect.com/science/article/pii/S0921818111002220. doi: 10.1016/J.GLOPLACHA.2011.12.003.

Thieulot, C. (2011). FANTOM: Two- and three-dimensional numerical modelling of creeping flows for the solution of geological problems. *Physics of the Earth and Planetary Interiors, 188,* 47–68. URL: https://www.sciencedirect.com/science/article/pii/S0031920111001336?via%3Dihub. doi: 10.1016/J.PEPI.2011.06.011.

Van Wijk, J. W., & Cloetingh, S. A. P. L. (2002). Basin migration caused by slow lithospheric extension. *Earth and Planetary Science Letters, 198,* 275–288. doi: 10.1016/S0012-821X(02)00560-5.

Vogt, K., Willingshofer, E., Matenco, L., Sokoutis, D., & Cloetingh, S. (2018). The role of lateral strength contrasts in orogenesis: A 2D numerical study. *Tectonophysics, 746,* 549–561. URL: https://www.sciencedirect.com/science/article/pii/S0040195117303293#bb0100. doi: 10.1016/J.TECTO.2017.08.010.

Watremez, L., Burov, E., D'Acremont, E., Leroy, S., Huet, B., Le Pourhiet, L., & Bellahsen, N. (2013). Buoyancy and localizing properties of continental mantle lithosphere: Insights from thermomechanical models of the eastern Gulf of Aden. *Geochemistry, Geophysics, Geosystems, 14,* 2800–2817. URL: http://doi.wiley.com/10.1002/ggge.20179. doi:

10.1002/ggge.20179.

Weissel, J. K., & Karner, G. D. (1989). Flexural uplift of rift flanks due to mechanical unloading of the lithosphere during extension. *Journal of Geophysical Research: Solid Earth, 94,* 13919–13950.

Wernicke, B. (1985). Uniform-sense normal simple shear of the continental lithosphere. *Canadian Journal of Earth Sciences, 22,* 108–125. URL: http://www.nrcresearchpress.com/doi/abs/10.1139/e85-009. doi: 10.1139/e85-009.

White, R., & McKenzie, D. (1989). Magmatism at rift zones: The generation of volcanic continental margins and flood basalts. *Journal of Geophysical Research, 94,* 7685. URL: http://doi.wiley.com/10.1029/JB094iB06p07685. doi: 10.1029/JB094iB06p07685.

van Wijk, J., Huismans, R. S., ter Voorde, M., & Cloetingh, S. A. P. L. (2001). Melt generation at volcanic margins: no need for a plume. *Geophysical Research Letters, 28,* 3995–3998.

Withjack, M. O., Schilsche, R. W., & Olsen, P. E. (2012). Development of the passive margin of eastern North America: Mesozoic rifting, igneous activity, and breakup. In D. G. Roberts, & A. W. Bally (Eds.), *Regional Geology and Tectonics: Phanerozoic Rift Systems and Sedimentary Basins* chapter 13. (pp. 301–335). Elsevier. doi: 10.1016/B978.

Xie, X. N., Müller, R. D., Li, S., Gong, Z., & Steinberger, B. (2006). Origin of anomalous subsidence along the Northern South China Sea margin and its relationship to dynamic topography. *Marine and Petroleum Geology, 23,* 745–765. doi: 10.1016/j.marpetgeo.2006.03.004.

Appendix A. Supplementary Model Results

Figure A.15: Top panels: surface (magenta curve), top basement and Moho topography (black curves) at the end of the necking phase (i.e. when the crust is thinned to 10 km). The space between the magenta and top basement curves represents sediments. The horizontal blue line corresponds to the isobath 0 km. The 500 °C (and in some panels the 1300 °C) isotherms are plotted in red. Bottom panels: evolution of surface topography with time along the model.

Figure A.16: a) Evolution of the total accommodation space and b) total emerged area with time along the all models. Accommodation space and emerged area are corrected from the initial topography of the model, so that the graphs display how much additional accommodation space and emerged area are created with time.

Figure A.17: Top panels: Difference between the initial and final temperature within the model at the end of the necking phase; temperature difference accounts for diffusion, production and advection of heat. The green lines represent the Moho and the initial lithosphere-asthenosphere boundary. Bottom panels: Model temperature at the end of the necking phase; the cyan lines represent the top basement, Moho and the initial lithosphere–asthenosphere boundary; dark blue lines represent selected model isotherms. Arrows in insets of Models D3–D6 and W3–W6 indicate the piece of mantle that keeps an elevated temperature with respect to its initial state.

Figure A.18: a–l: Surface heat flow with time along the different models. The contour lines represent crustal thickness isopachs: 15 km (black), 20 km (magenta) and 25 km (yellow).

Figure A.19: Top panels: surface (magenta curve), top basement and Moho topography (black curves) at the end of the necking phase (i.e. when the crust is thinned to 10 km). The space between the magenta and top basement curves represents sediments. The horizontal blue line corresponds to the isobath 0 km. The 500 °C (and in some panels the 1300 °C) isotherms are plotted in red. Bottom panels: evolution of surface topography with time along the model. Strain soft.: Strain softening.

Figure A.20: Top panels: Difference between the initial and final temperature within the model at

the end of the necking phase; temperature difference accounts for diffusion, production and advection of heat. The green lines represent the Moho and the initial lithosphere-asthenosphere boundary. Bottom panels: Model temperature at the end of the necking phase; the cyan lines represent the top basement, Moho and the initial lithosphere–asthenosphere boundary; dark blue lines represent selected model isotherms. Strain soft.: Strain softening.

Figure A.21: a–l: Surface heat flow with time along the different models. The contour lines represent crustal thickness isopachs: 15 km (black), 20 km (magenta) and 25 km (blue). Strain soft.: Strain softening.

Highlights

- Rift systems show complex topographic and thermal evolutions during the necking phase
- Mechanical decoupling between the crust and mantle largely controls these evolutions
- Efficient decoupling enables uplift of distal domains during advanced necking stages
- Efficient decoupling produces differential lithosphere heating/cooling during necking
- As much accommodation space as emerged space is created during the necking phase

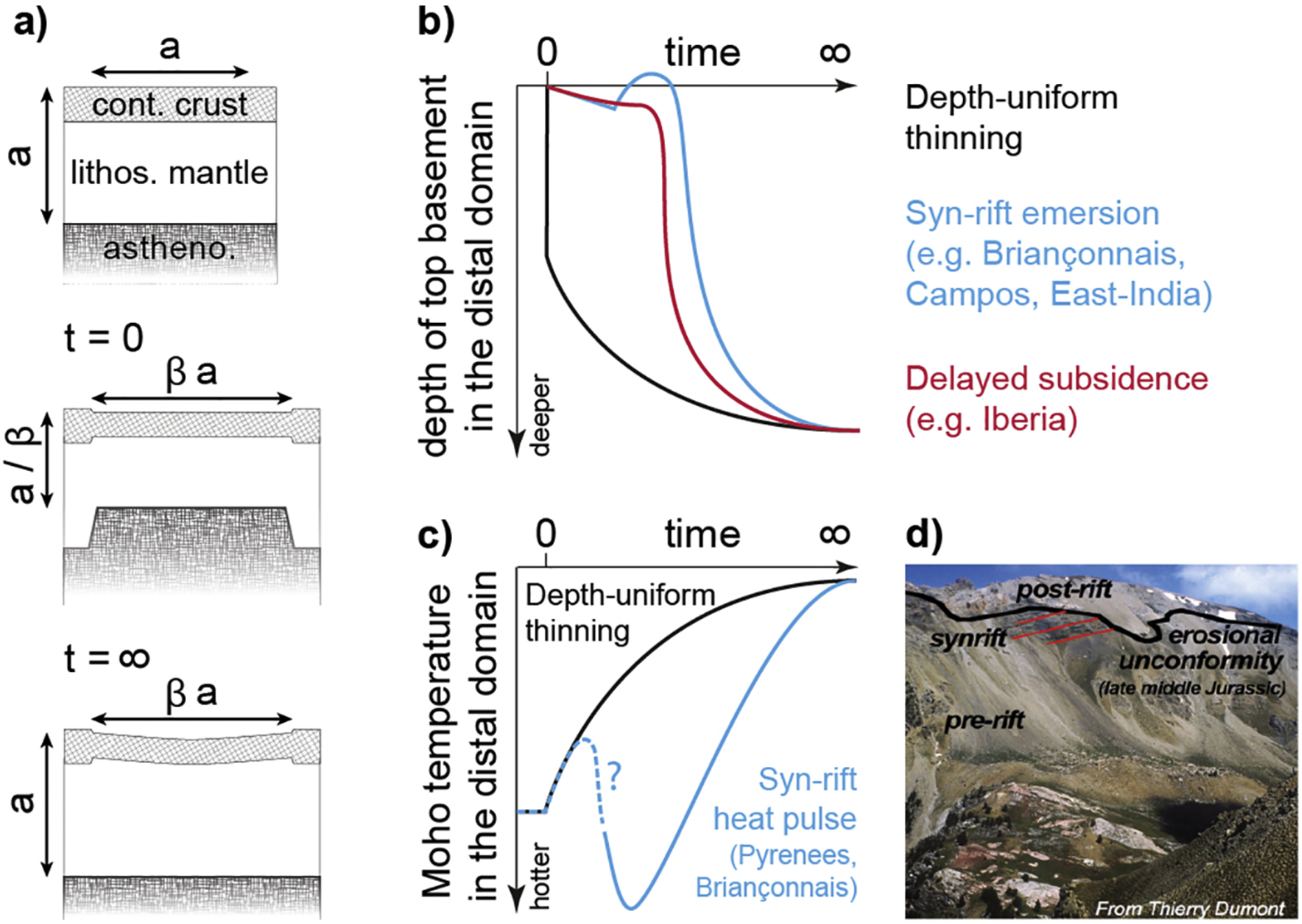
a)
a
a
cont. crust
lithos. mantle
astheno.
t = 0
β a
a / β
t = ∞
β a
a
b)
0
time
∞
depth of top basement in the distal domain
deeper
Depth-uniform thinning
Syn-rift emersion (e.g. Briançonnais, Campos, East-India)
Delayed subsidence (e.g. Iberia)
c)
0
time
∞
Moho temperature in the distal domain
hotter
Depth-uniform thinning
?
Syn-rift heat pulse (Pyrenees, Briançonnais)
d)
post-rift
synrift
erosional unconformity
(late middle Jurassic)
pre-rift
From Thierry Dumont

Figure 1

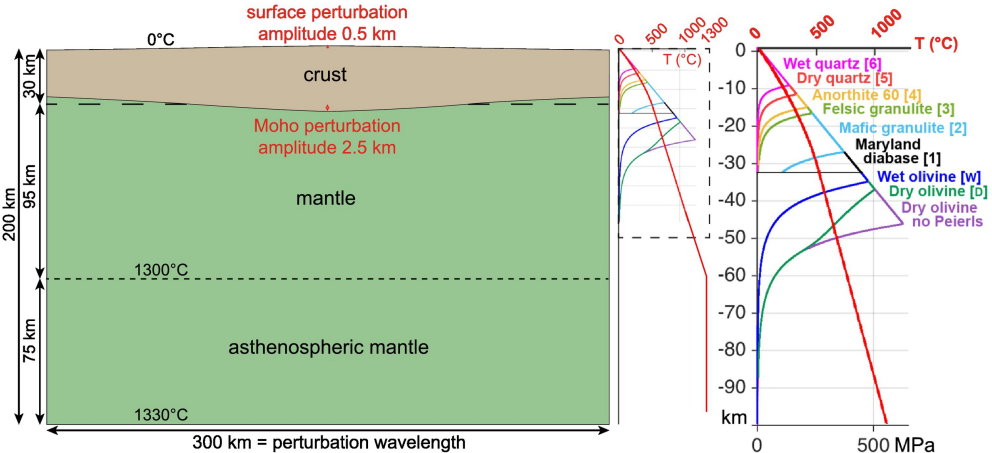
surface perturbation
amplitude 0.5 km
0°C
crust
30 km
Moho perturbation
amplitude 2.5 km
mantle
95 km
200 km
1300°C
asthenospheric mantle
75 km
1330°C
300 km = perturbation wavelength
0
500
1000
1300
T (°C)
T (°C)
Wet quartz [6]
Dry quartz [5]
Anorthite 60 [4]
Felsic granulite [3]
Mafic granulite [2]
Maryland
diabase [1]
Wet olivine [w]
Dry olivine [d]
Dry olivine
no Peierls
0
-10
-20
-30
-40
-50
-60
-70
-80
-90
km
0
500 MPa

Figure 2

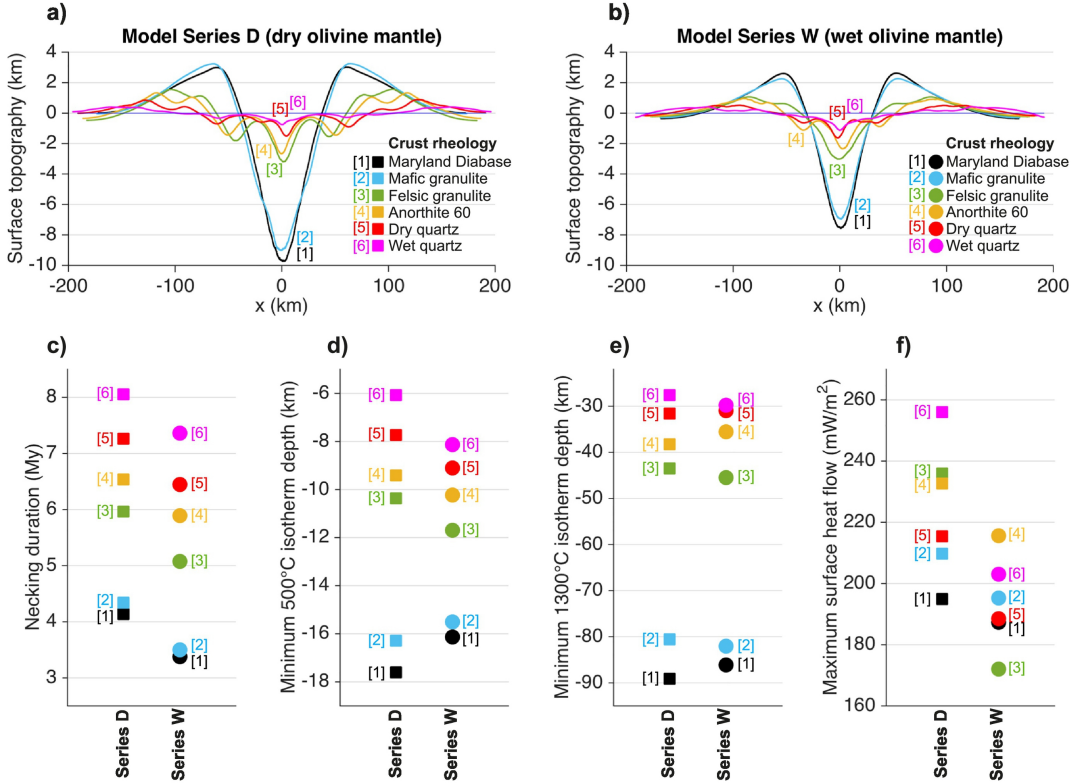
a)
Model Series D (dry olivine mantle)
Surface topography (km)
x (km)
Crust rheology
[1] Maryland Diabase
[2] Mafic granulite
[3] Felsic granulite
[4] Anorthite 60
[5] Dry quartz
[6] Wet quartz
b)
Model Series W (wet olivine mantle)
Surface topography (km)
x (km)
Crust rheology
[1] Maryland Diabase
[2] Mafic granulite
[3] Felsic granulite
[4] Anorthite 60
[5] Dry quartz
[6] Wet quartz
c)
Necking duration (My)
Series D
Series W
d)
Minimum 500°C isotherm depth (km)
Series D
Series W
e)
Minimum 1300°C isotherm depth (km)
Series D
Series W
f)
Maximum surface heat flow (mW/m2)
Series D
Series W

Figure 3

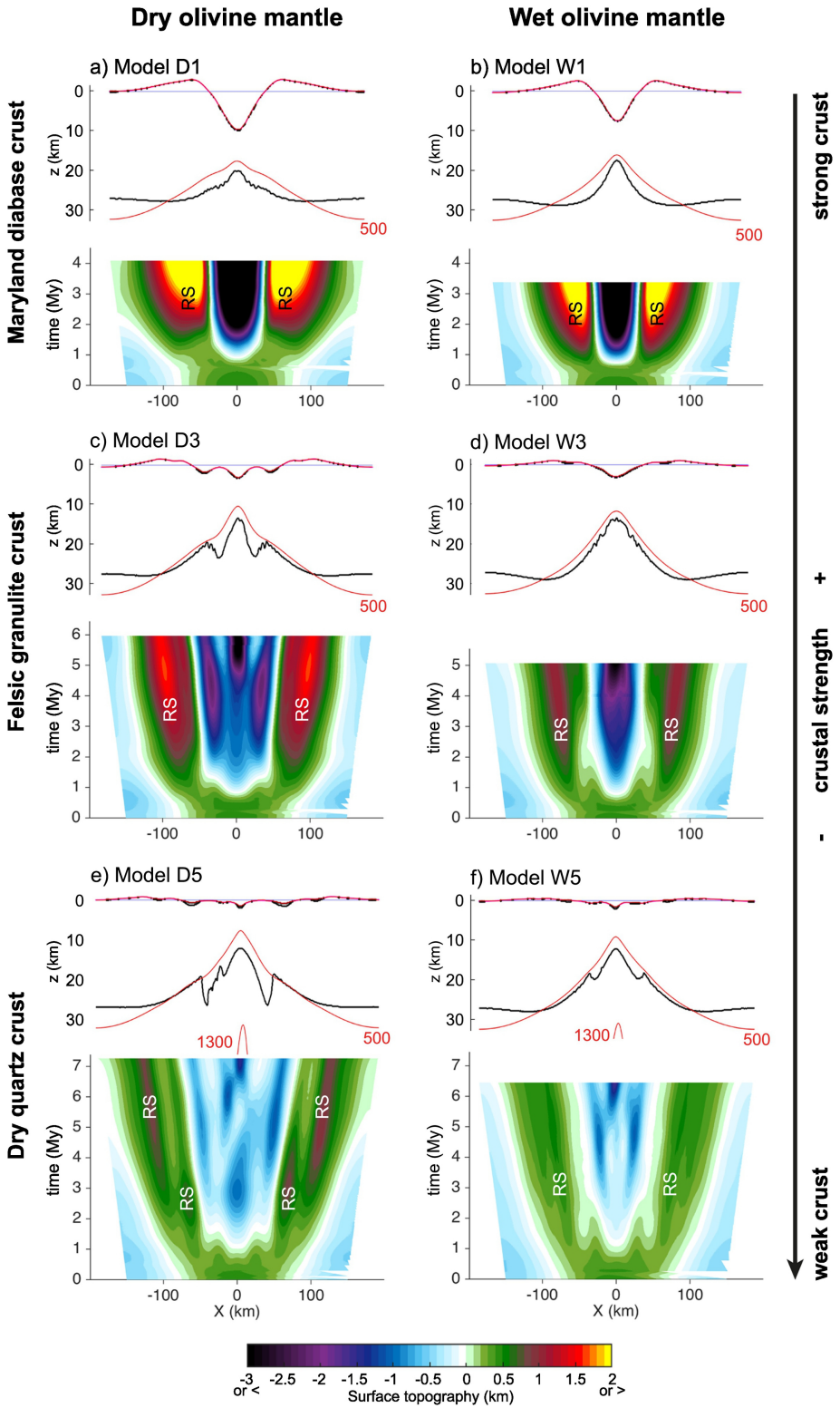
Dry olivine mantle
Wet olivine mantle
a) Model D1
b) Model W1
c) Model D3
d) Model W3
e) Model D5
f) Model W5
Maryland diabase crust
Felsic granulite crust
Dry quartz crust
z (km)
time (My)
RS
500
1300
X (km)
strong crust
crustal strength
weak crust
+
-
Surface topography (km)
-3 or <
-2.5
-2
-1.5
-1
-0.5
0
0.5
1
1.5
2 or >

Figure 4

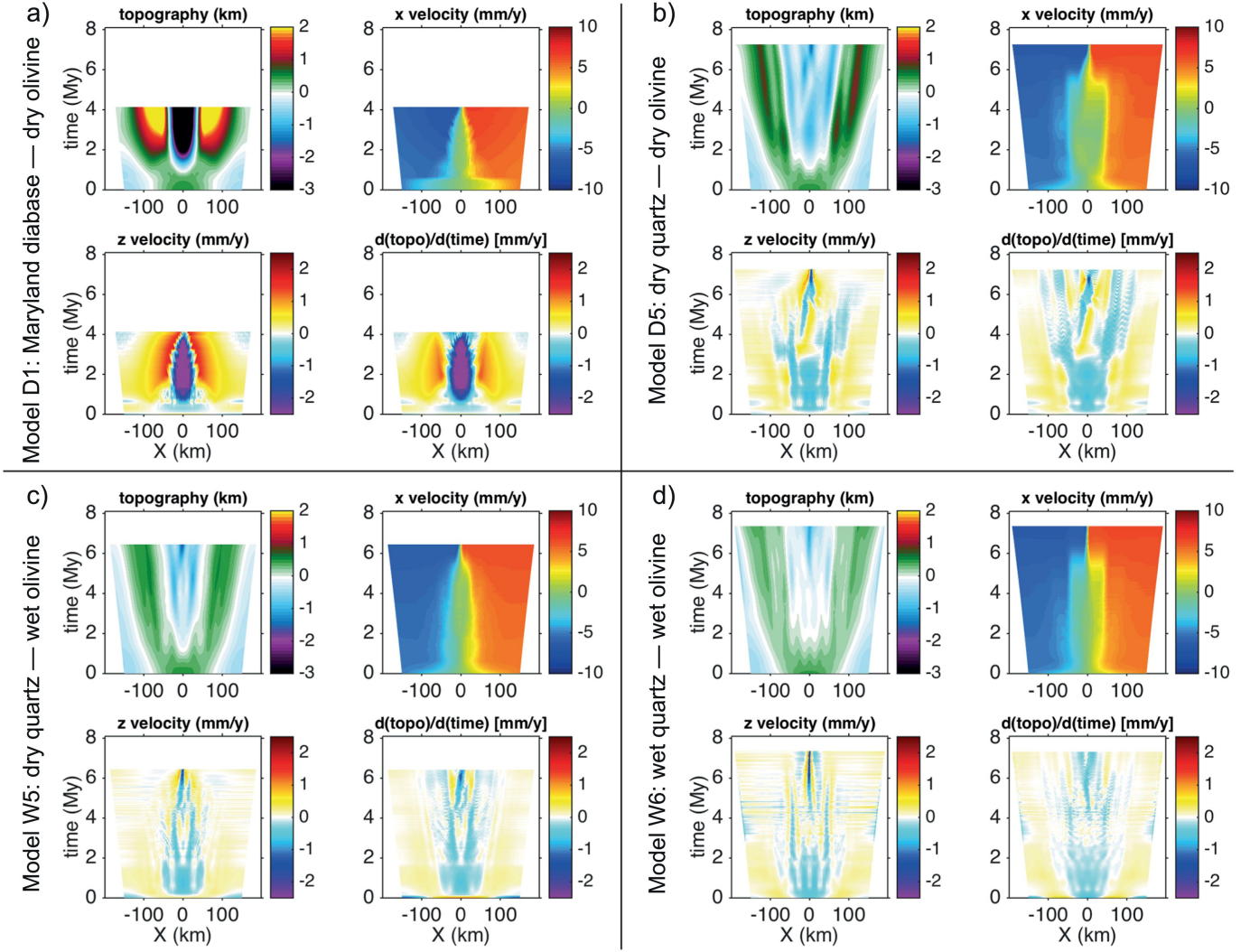
a)
Model D1: Maryland diabase — dry olivine
topography (km)
x velocity (mm/y)
z velocity (mm/y)
d(topo)/d(time) [mm/y]
time (My)
X (km)
b)
Model D5: dry quartz — dry olivine
c)
Model W5: dry quartz — wet olivine
d)
Model W6: wet quartz — wet olivine

Figure 5

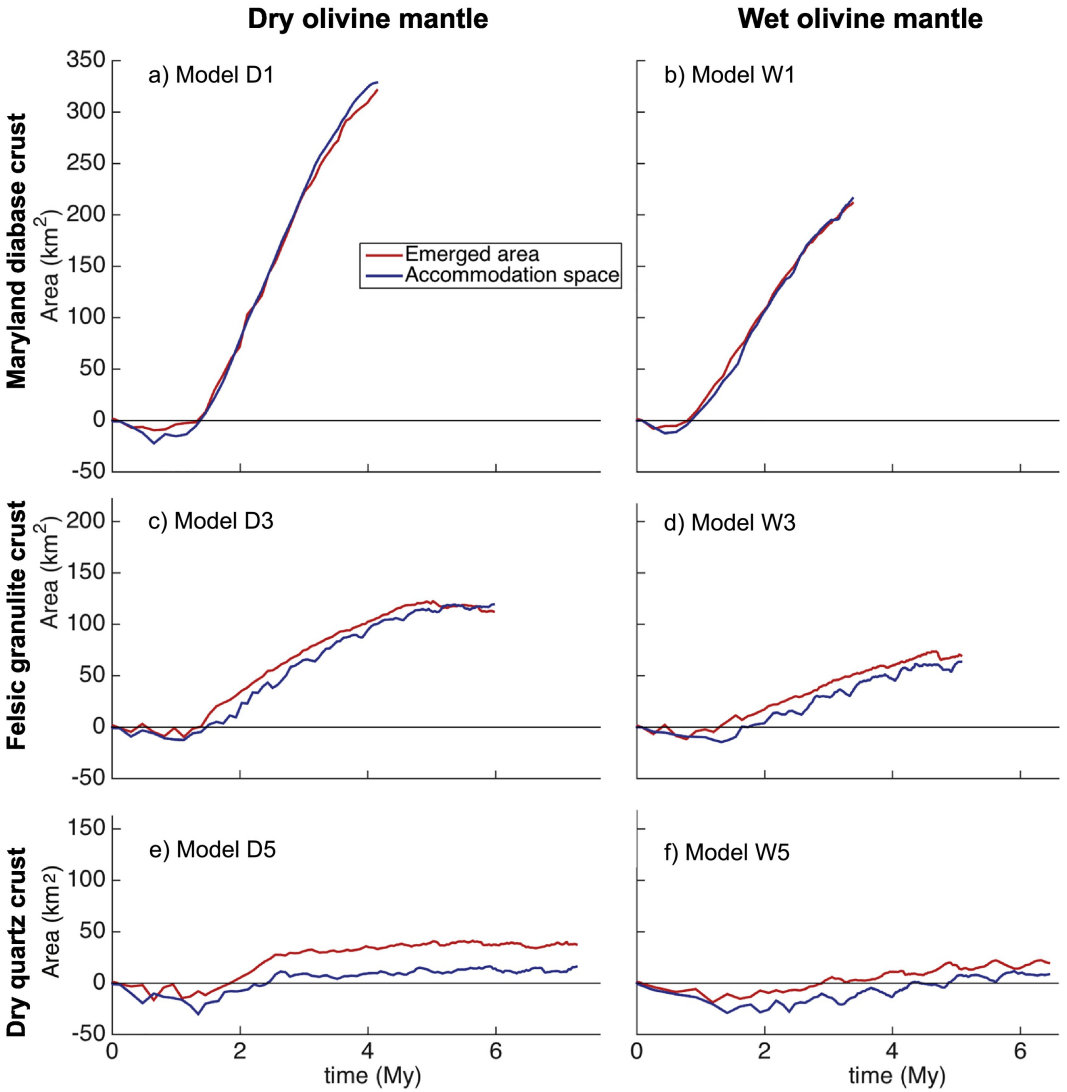
Dry olivine mantle
Wet olivine mantle
Maryland diabase crust
Felsic granulite crust
Dry quartz crust
a) Model D1
b) Model W1
c) Model D3
d) Model W3
e) Model D5
f) Model W5
Area (km2)
Emerged area
Accommodation space
time (My)

Figure 6

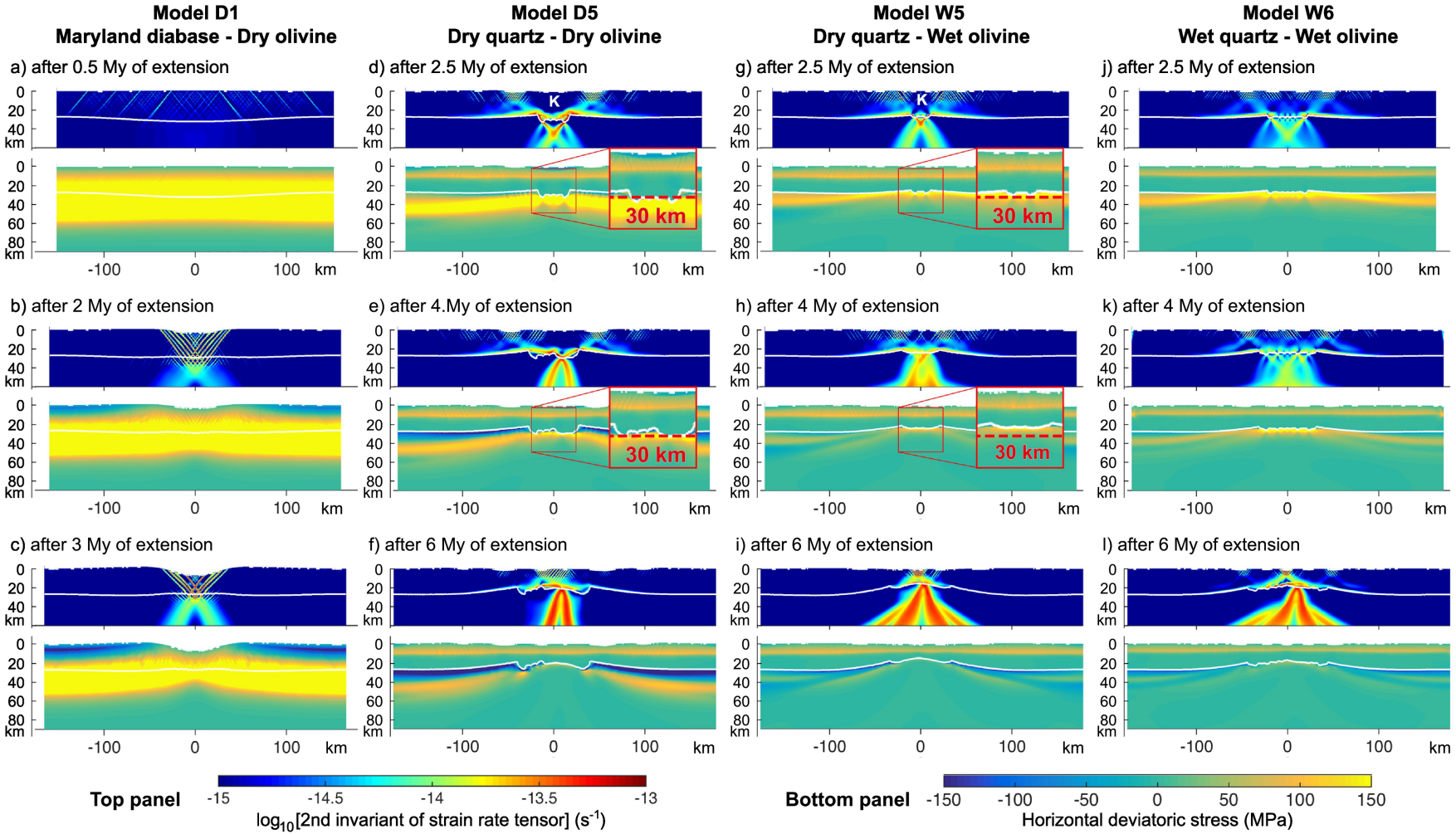
Model D1
Maryland diabase - Dry olivine
Model D5
Dry quartz - Dry olivine
Model W5
Dry quartz - Wet olivine
Model W6
Wet quartz - Wet olivine
a) after 0.5 My of extension
b) after 2 My of extension
c) after 3 My of extension
d) after 2.5 My of extension
e) after 4.My of extension
f) after 6 My of extension
g) after 2.5 My of extension
h) after 4 My of extension
i) after 6 My of extension
j) after 2.5 My of extension
k) after 4 My of extension
l) after 6 My of extension
K
30 km
0
20
40
60
80
km
-100
0
100
km
Top panel
-15
-14.5
-14
-13.5
-13
log10[2nd invariant of strain rate tensor] (s-1)
Bottom panel
-150
-100
-50
0
50
100
150
Horizontal deviatoric stress (MPa)

Figure 7

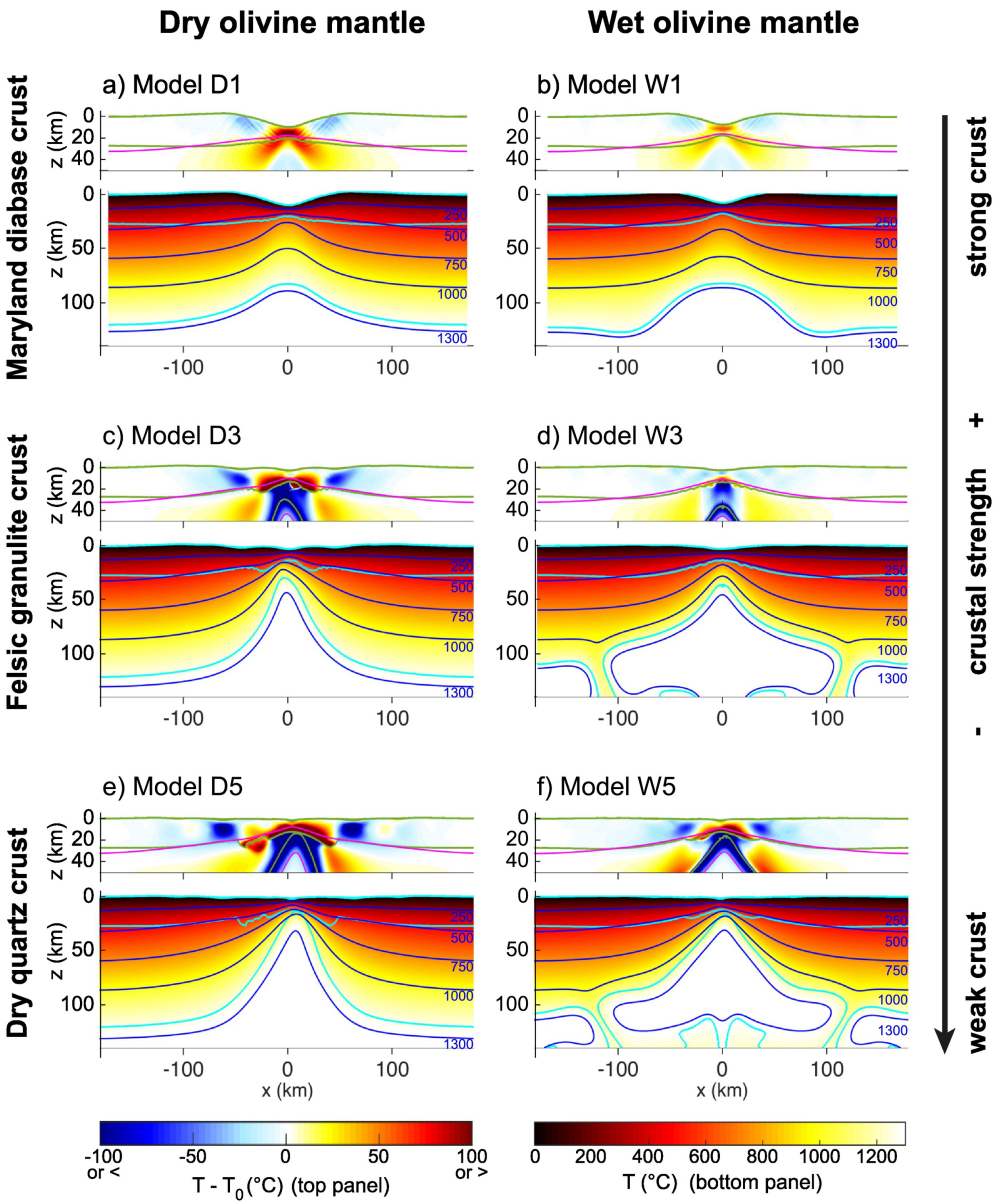
Dry olivine mantle
Wet olivine mantle
Maryland diabase crust
Felsic granulite crust
Dry quartz crust
a) Model D1
b) Model W1
c) Model D3
d) Model W3
e) Model D5
f) Model W5
z (km)
x (km)
250
500
750
1000
1300
strong crust
crustal strength
weak crust
+
-
-100 or <
-50
0
50
100 or >
T - T0 (°C) (top panel)
0
200
400
600
800
1000
1200
T (°C) (bottom panel)

Figure 8

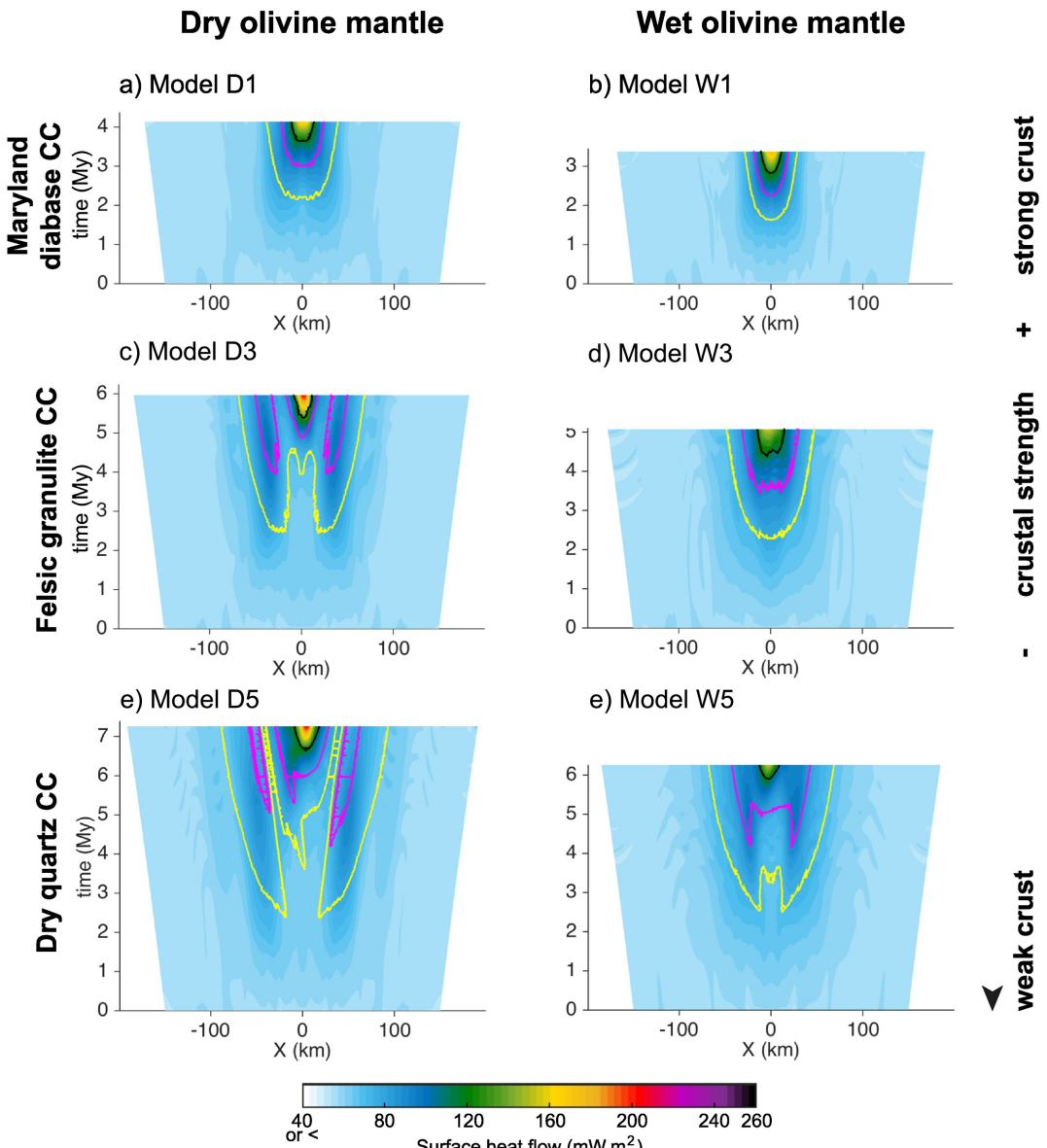
Dry olivine mantle
Wet olivine mantle
a) Model D1
b) Model W1
c) Model D3
d) Model W3
e) Model D5
e) Model W5
Maryland diabase CC
Felsic granulite CC
Dry quartz CC
time (My)
X (km)
-100
0
100
+
crustal strength
-
strong crust
weak crust
40 or <
80
120
160
200
240
260
Surface heat flow (mW.m^2)

Figure 9

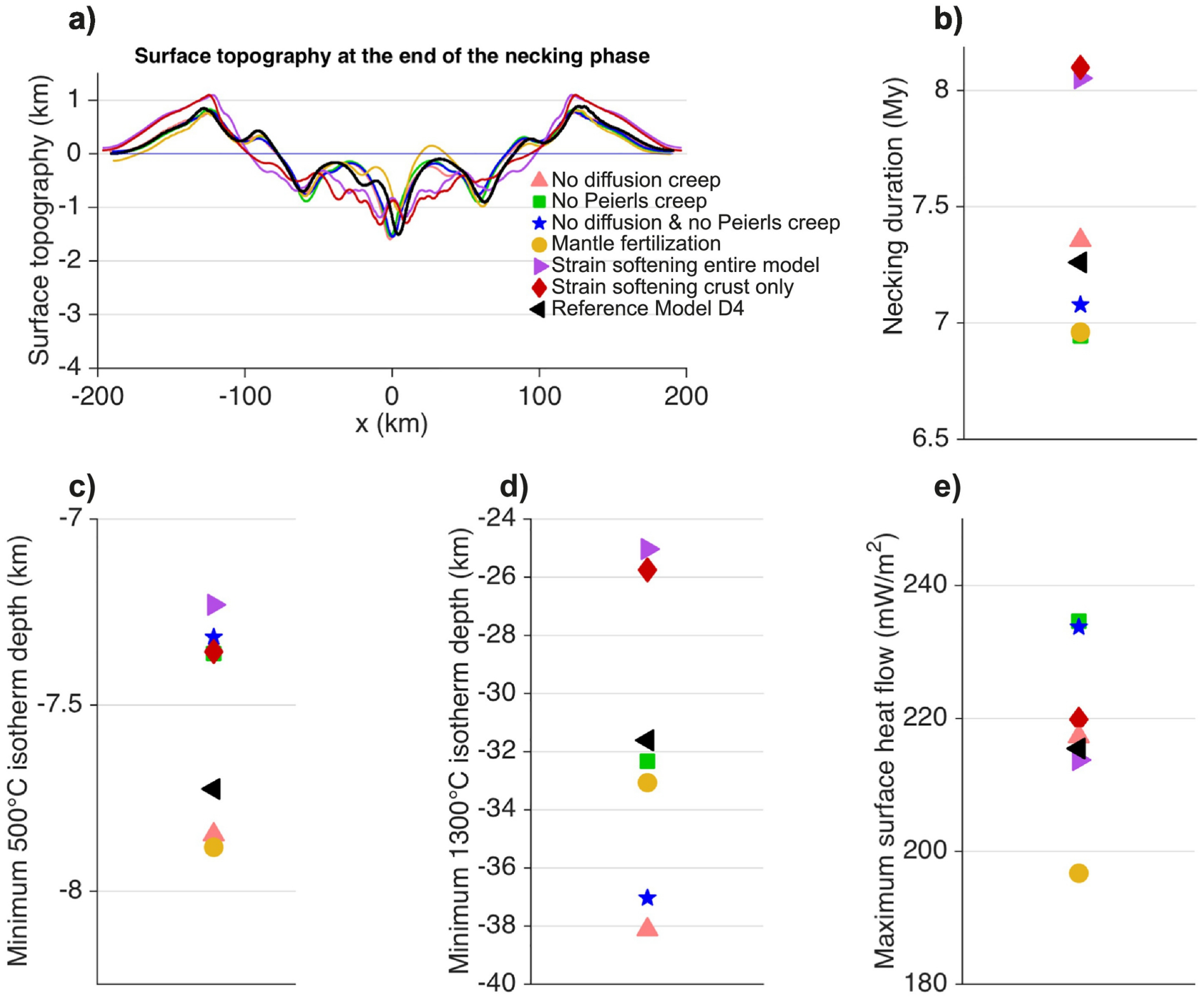
a)
Surface topography at the end of the necking phase
Surface topography (km)
1
0
-1
-2
-3
-4
-200
-100
0
100
200
x (km)
No diffusion creep
No Peierls creep
No diffusion & no Peierls creep
Mantle fertilization
Strain softening entire model
Strain softening crust only
Reference Model D4
b)
Necking duration (My)
8
7.5
7
6.5
c)
Minimum 500°C isotherm depth (km)
-7
-7.5
-8
d)
Minimum 1300°C isotherm depth (km)
-24
-26
-28
-30
-32
-34
-36
-38
-40
e)
Maximum surface heat flow (mW/m2)
240
220
200
180

Figure 10

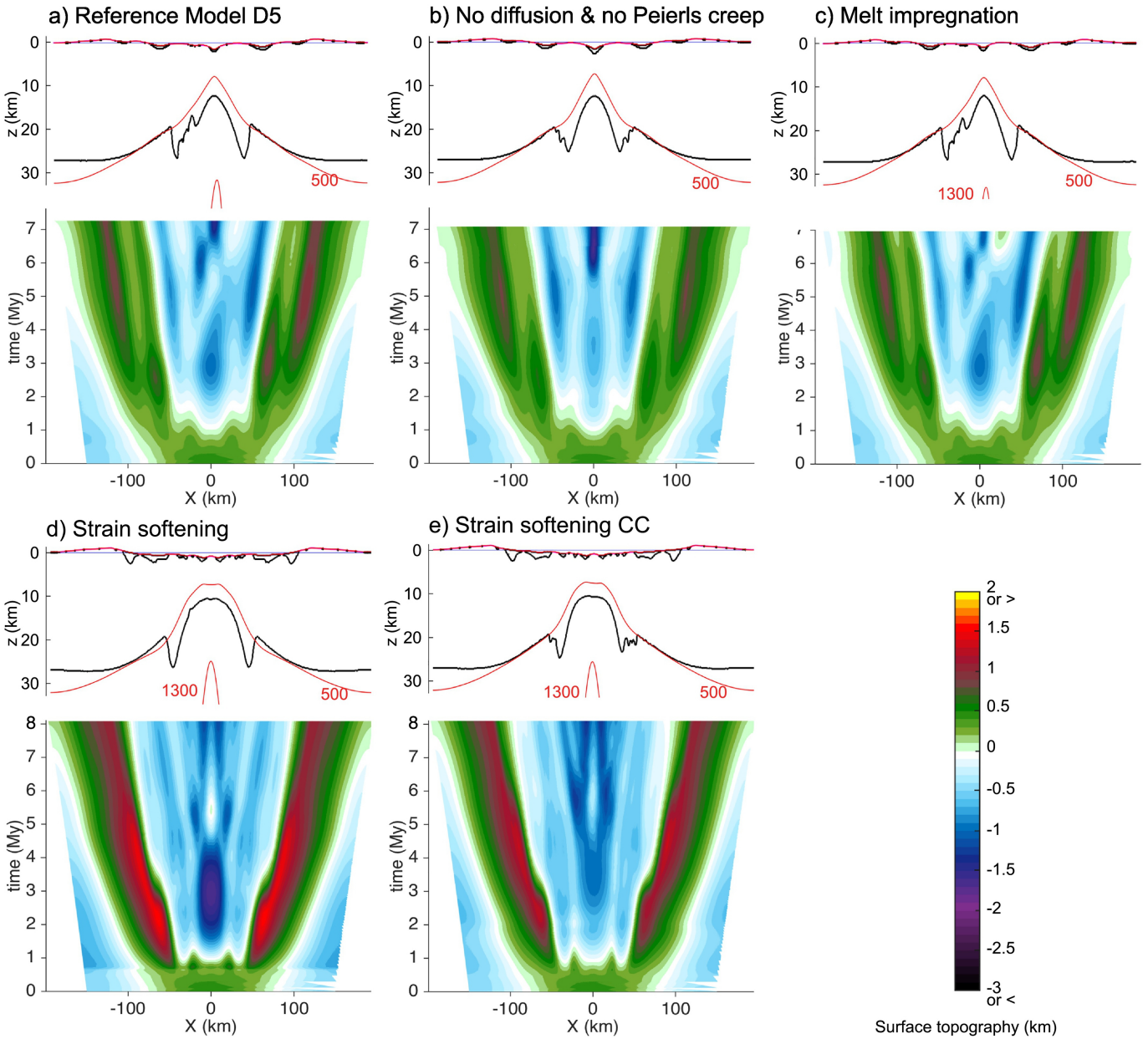
a) Reference Model D5
b) No diffusion & no Peierls creep
c) Melt impregnation
d) Strain softening
e) Strain softening CC
z (km)
time (My)
X (km)
500
1300
Surface topography (km)
2 or >
1.5
1
0.5
0
-0.5
-1
-1.5
-2
-2.5
-3 or <

Figure 11

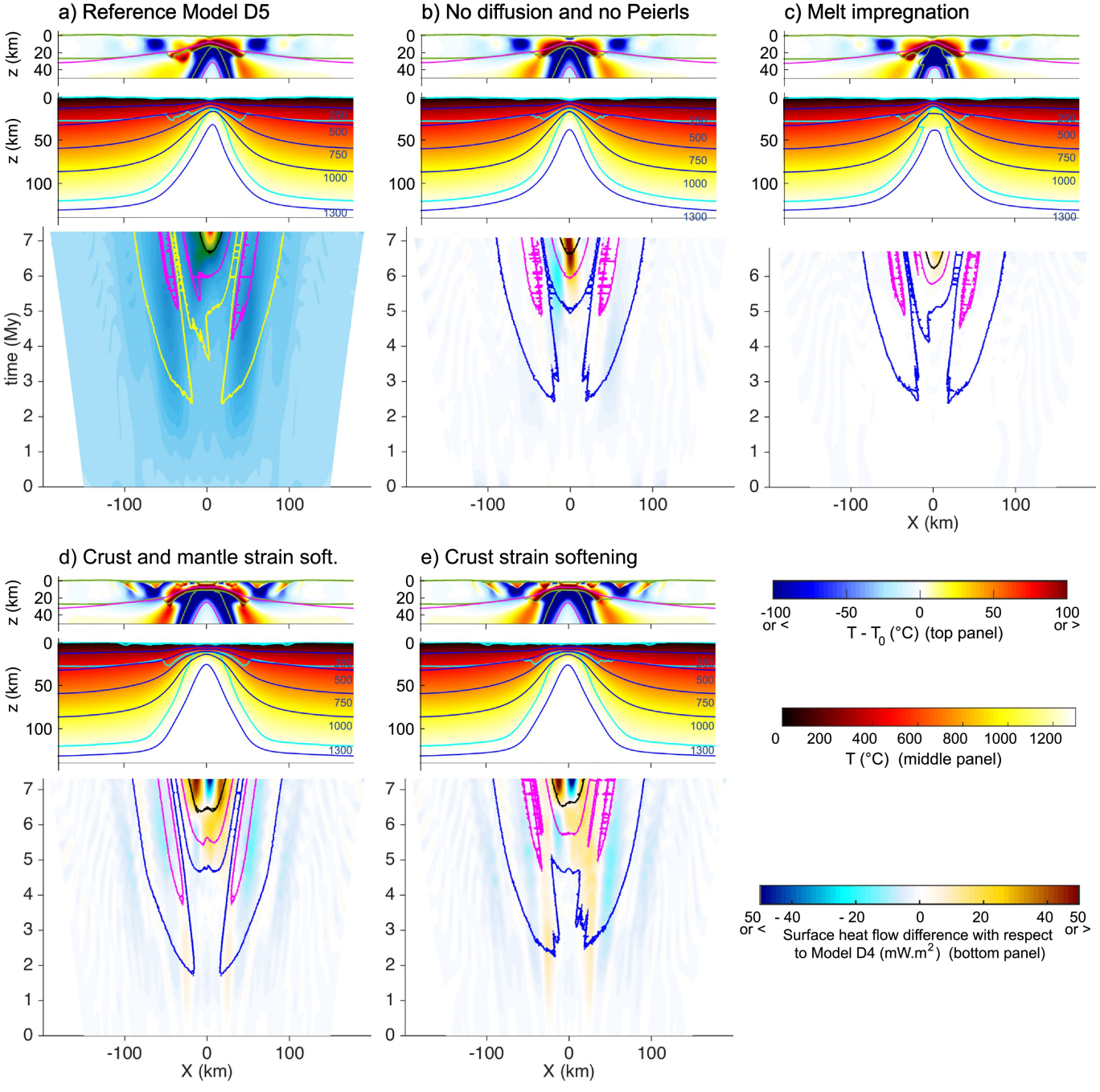
a) Reference Model D5
b) No diffusion and no Peierls
c) Melt impregnation
d) Crust and mantle strain soft.
e) Crust strain softening
z (km)
time (My)
X (km)
250
500
750
1000
1300
-100 or < -50 0 50 100 or >
T - T0 (°C) (top panel)
0 200 400 600 800 1000 1200
T (°C) (middle panel)
50 or < - 40 - 20 0 20 40 50 or >
Surface heat flow difference with respect to Model D4 (mW.m2) (bottom panel)

Figure 12

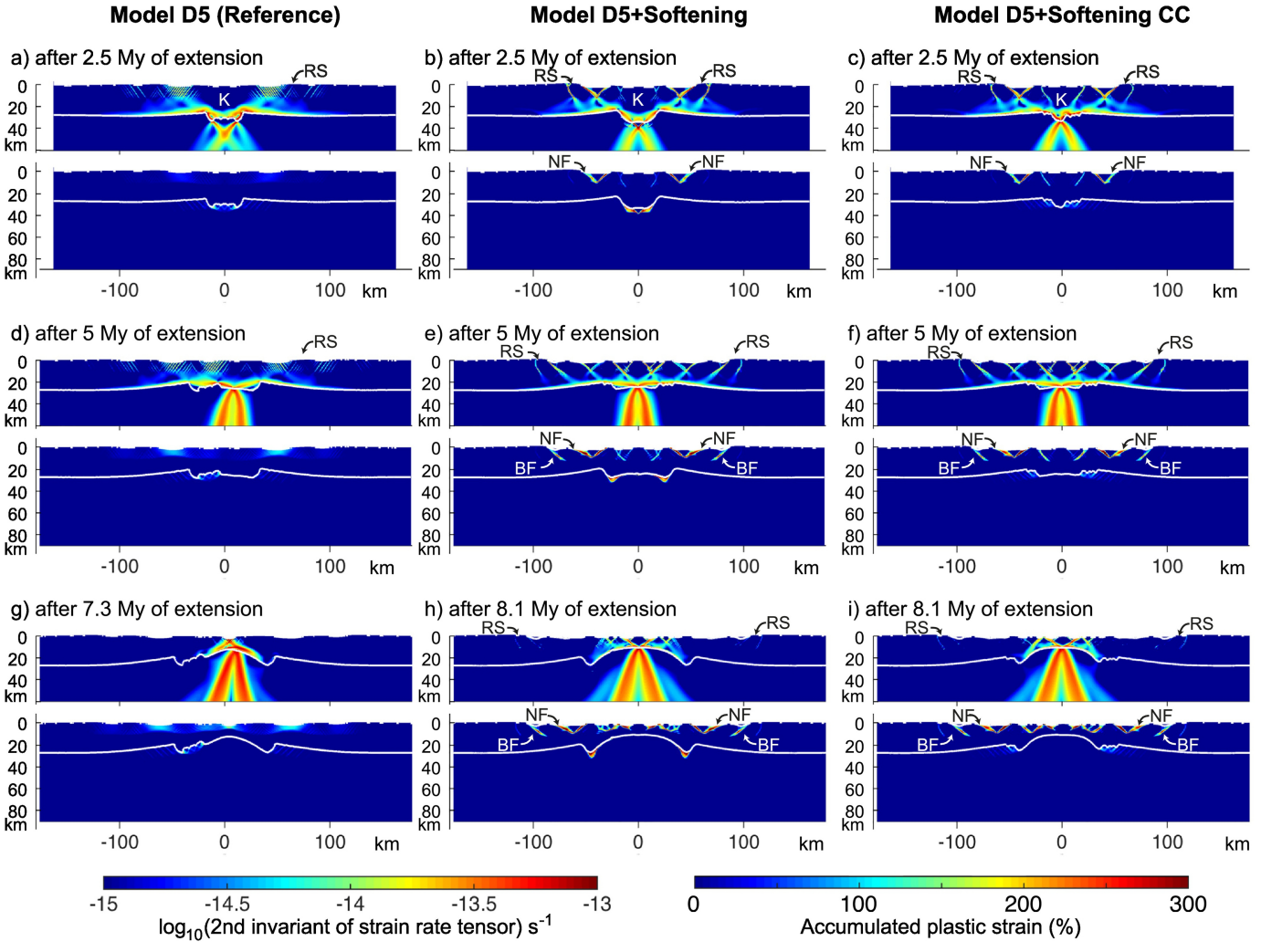
Model D5 (Reference)
Model D5+Softening
Model D5+Softening CC
a) after 2.5 My of extension
b) after 2.5 My of extension
c) after 2.5 My of extension
d) after 5 My of extension
e) after 5 My of extension
f) after 5 My of extension
g) after 7.3 My of extension
h) after 8.1 My of extension
i) after 8.1 My of extension
RS
K
NF
BF
0
20
40
60
80
km
-100
0
100
-15
-14.5
-14
-13.5
-13
log10(2nd invariant of strain rate tensor) s-1
0
100
200
300
Accumulated plastic strain (%)

Figure 13

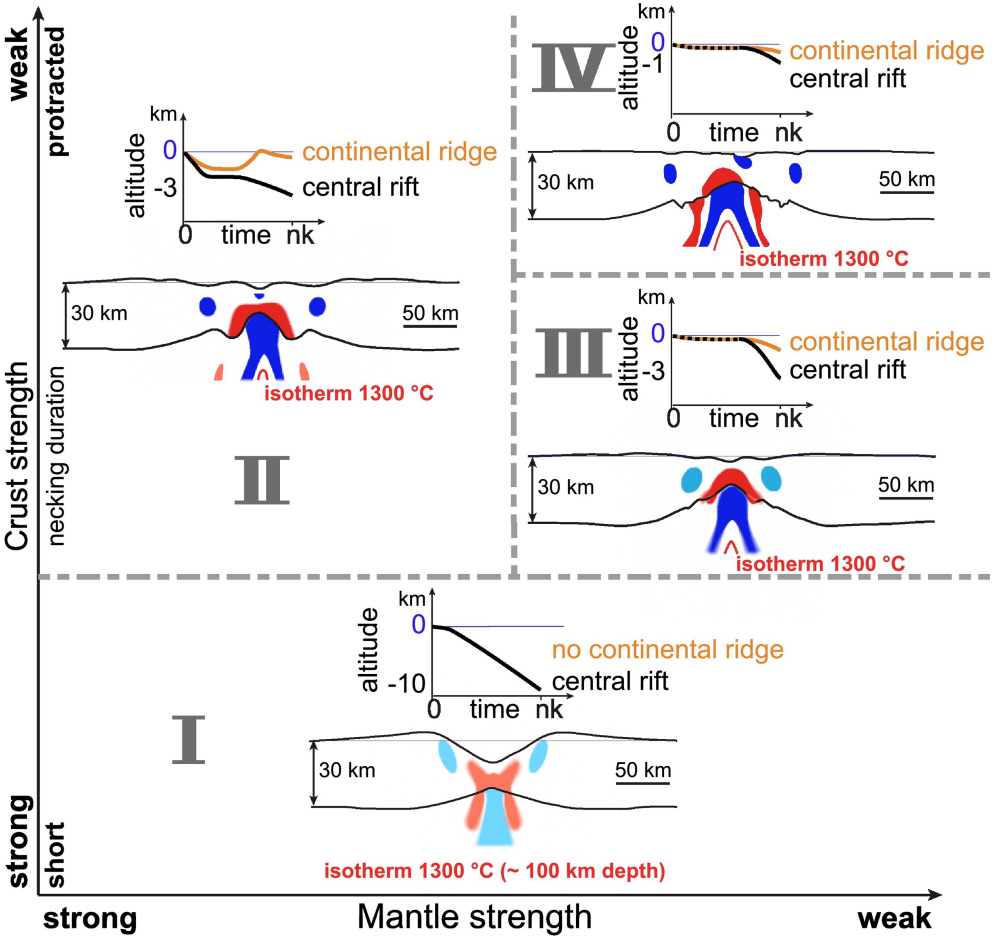
weak
protracted
Crust strength
necking duration
strong
short
strong
Mantle strength
weak
km
altitude
0
-3
continental ridge
central rift
0 time nk
30 km
50 km
isotherm 1300 °C
II
III
IV
km
altitude
0
-1
continental ridge
central rift
0 time nk
30 km
50 km
isotherm 1300 °C
km
altitude
0
-10
no continental ridge
central rift
0 time nk
I
30 km
50 km
isotherm 1300 °C (~ 100 km depth)

Figure 14